A&A 423, 867–880 (2004)
DOI: 10.1051/0004-6361:20035740

Astronomy & Astrophysics

The Luminosity–Metallicity relation of distant luminous infrared galaxies⋆,⋆⋆

Y. C. Liang[1,2], F. Hammer[1], H. Flores[1], D. Elbaz[3], D. Marcillac[3], and C. J. Cesarsky[4]

[1] GEPI, Observatoire de Paris, Section de Meudon, 92195 Meudon Cedex, France
e-mail: [Yanchun.Liang;francois.hammer]@obspm.fr
[2] National Astronomical Observatories, Chinese Academy of Sciences, No. 20A Datun Road, Chaoyang District, Beijing 100012, PR China
e-mail: ycliang@ns.bao.ac.cn
[3] CEA, Saclay-Service d'Astrophysique, Orme des Merisiers, 91191 Gif-sur-Yvette Cedex, France
[4] ESO, Karl-Schwarzschild Strasse 2, 85748 Garching bei Munchen, Germany

Received 25 November 2003 / Accepted 26 April 2004

Abstract. One hundred and five 15 μm-selected objects in three ISO (*Infrared Space Observatory*) deep survey fields (CFRS 3^h, UDSR and UDSF) are studied on the basis of their high-quality optical spectra with resolution $R > 1000$ from VLT/FORS2. ~92 objects (88%) have secure redshifts, ranging from 0 to 1.16 with a median value of $z_{\rm med} = 0.587$.
Considerable care is taken in estimating the extinction properties of individual galaxy, which can seriously affect diagnostic diagrams and estimates of star formation rates (SFRs) and of metal abundances. Two independent estimates of the extinction have been made, e.g. Balmer line ratio and energy balance between infrared (IR) and Hβ luminosities. For most of the sources, we find a good agreement between the two extinction coefficients (within ±0.64 rms in A_V, the extinction in V band), with median values of A_V(IR) = 2.36 and A_V(Balmer) = 1.82 for $z > 0.4$ luminous IR galaxies (LIRGs). At $z > 0.4$, our sample show many properties (IR luminosity, continuum color, ionization and extinction) strikingly in common with those of local (IRAS) LIRGs studied by Veilleux et al. (1995). Thus, our sample can provide a good representation of LIRGs in the distant Universe.
We confirm that most (>77%) ISO 15 μm-selected galaxies are dominated by star formation. Oxygen abundances in interstellar medium in the galaxies are estimated from the extinction-corrected "strong" emission line ratios (e.g. [O II]/Hβ, [O III]/Hβ and [O III]/[O II]). The derived 12+log(O/H) values range from 8.36 to 8.93 for the $z > 0.4$ galaxies with a median value of 8.67. Distant LIRGs present a metal content less than half of that of the local bright disks (i.e. L^*). Their properties can be reproduced with infall models although one has to limit the infall time to avoid overproduction of metals at late times. The models predict that total masses (gas + stars) of the distant LIRGs are from 10^{11} $M_\odot$ to $\leq 10^{12}$ $M_\odot$. A significant fraction of distant large disks are indeed LIRGs. Such massive disks could have formed ~50% of their metals and stellar masses since $z \sim 1$.

Key words. galaxies: abundances – galaxies: evolution – galaxies: ISM – galaxies: photometry – galaxies: spiral – galaxies: starburst

1. Introduction

The IRAS all-sky survey detected tens of thousands of galaxies with far-infrared (far-IR) radiation luminosities from less than 10^6 $L_\odot$ to ~10^{13} $L_\odot$ up to a moderate redshift ($z \sim 0.3$). However, luminous infrared galaxies (LIRGs) are not typical of local galaxy population, and they account for only ~2% of the local bolometric luminosity density (Soifer et al. 1987; Sanders & Mirabel 1996).

However, the COsmic Background Explorer (COBE) observations imply that there likely exists a very significant contribution of dust-obscured star formation at high redshifts (Puget et al. 1996; Genzel & Cesarsky 2000). The ISO made it possible to study the infrared emission of galaxies at $z \geq 0.5$, which plays an important role in understanding the co-moving star formation density evolution with look-back time. The ISO mid infrared camera (ISOCAM) (Cesarsky et al. 1996) is ~10^3 times more sensitive and has 60 times higher spatial resolution than IRAS. The mid-IR ISOCAM 15 μm source counts provide evidence for strong IR light density evolution, as revealed by the strong excess of 15 μm counts above the predictions of non-evolution models at sub-mJy (Elbaz et al. 1999; Aussel et al. 1999). The cosmic infrared background resolved

⋆ Based on observations collected with the ESO Very Large Telescope at the Paranal Observatory (66.A-0599(A)) and with ISOCAM Deep Survey and ISO-CFRS follow-up.
⋆⋆ Table 1–7 are only available in electronic form at http://www.edpsciences.org

by ISOCAM shows that the co-moving density of infrared light due to the luminous IR galaxies ($L_{\rm IR} \geq 10^{11}\ L_{\odot}$) was more than 40 times larger at $z \sim 1$ than today (Elbaz et al. 2002). The main driver for this evolution is the luminous infrared starburst galaxies seen by ISO at $z > 0.4$, which form stars at a rate of more than 50 $M_{\odot}\ {\rm yr}^{-1}$ (Flores et al. 1999).

Based on the correlation analysis of deep X-ray and mid-IR observations in Lockman Hole and Hubble Deep Field North (HDF-N), Fadda et al. (2002) found that the active galactic nuclei (AGN) contribution to the 15 μm background is only 17 ± 2%. They concluded that the population of IR luminous galaxies detected in the ISOCAM deep surveys, and the cosmic infrared background sources themselves, are mostly dust-obscured starbursts (also see Elbaz et al. 2002). Reviews of extragalactic results from ISO can be found in Genzel & Cesarsky (2000), Franceschini et al. (2001) and Elbaz & Cesarsky (2003).

Recently, Flores et al. (2004a) studied the interstellar extinction and SFRs of 16 luminous infrared galaxies in Canada-France Redshift Survey (CFRS) $3^{\rm h}$ and $14^{\rm h}$ fields using the spectra from the European Southern Observatory (ESO) Very Large Telescope (VLT) and Canada-France-Hawaii Telescope (CFHT). They found that the extinction coefficients obtained from Hγ/Hβ (using the VLT/FORS2 or CFHT spectra) and Hα/Hβ (combining the VLT/FORS2 and VLT/ISAAC spectra) are in agreement, and that SFRs derived from Hα are consistent with those from infrared luminosities, except for the galaxies near the ultra luminous IR galaxy (ULIRG) regime ($L_{\rm IR} > 10^{12}\ L_{\odot}$).

Spectrophotometric properties of IRAS galaxies have been studied in detail, providing a full diagnostic of their ISM properties (Veilleux et al. 1995, hereafter V95; Kim et al. 1995). However, at higher redshifts, studies of ISOCAM sources have mostly focused on source counts and SFRs. Very little is known about chemical properties of distant LIRGs, including their metal content, and the main objective of this paper is to fill this gap.

In the local Universe, metallicity is well correlated with the absolute luminosity (stellar mass) of galaxies over a wide magnitude range (e.g. 7−9 mag) (Zaritsky et al. 1994; Richer & McCall 1995; Telles & Terlevich 1997; Contini et al. 2002; Melbourne & Salzer 2002; Lamareille et al. 2004). Some results have been obtained on the luminosity–metallicity (L–Z) relations in the intermediate-redshift Universe. Kobulnicky & Zaritsky (1999) found that the L–Z relations of 14 intermediate-z emission line galaxies with $0.1 < z < 0.5$ are consistent with those of the local spiral and irregular galaxies studied by Zaritsky et al. (1994), Telles & Terlevich (1997) and Richer & McCall (1995). The 16 CFRS galaxies at $z \sim 0.2$ studied by Liang et al. (2004) fall well in the region occupied by the local spiral galaxies (from Zaritsky et al. 1994).

At higher redshifts, Kobulnicky et al. (2003) have obtained the L–Z relations of 64 galaxies from the Deep Groth Strip Survey (DGSS) which have been separated into three redshift ranges (z = 0.2−0.4, 0.4−0.6, and 0.6−0.82). In the highest redshift bin galaxies are brighter by ∼1 mag relatively to those in the lowest redshift bin and brighter by ∼2.4 mag compared to the local ($z < 0.1$) field galaxies (from Kennicutt 1992a,b, hereafter K92, and Jansen et al. 2000a,b, hereafter J20). Such a result is confirmed by Maier et al. (2004). These studies contrast with the results of Lilly et al. (2003), who have found that the L–Z relation of most of their 66 CFRS galaxies with $0.5 < z < 1$ is similar to that of the local galaxies from J20. However, Lilly et al. (2003) have assumed a constant $A_V = 1$ for accounting for dust extinction. In this study, we investigate the L–Z relation for LIRGs in $z > 0.4$ Universe, after a detailed account for their dust extinction properties.

This paper is organized as it follows. In Sect. 2, we describe the sample selection, the observations and the data reduction and analysis, while the redshift distribution and the spectrophotometric properties are presented in Sect. 3. Sections 2 and 3 are aiming at assessing whether our resulting sample can be used to test the properties of distant LIRGs. Flux measurements, interstellar extinction and SFRs of the galaxies are shown in Sect. 4. It includes a detailed comparison between extinction parameter deduced from Balmer line ratio to that derived from mid-IR luminosity. In Sect. 5, we discuss the diagnostic diagrams to test the AGN contribution as well as the ionization properties. In Sect. 6, we present the luminosity-metallicity relation (based on oxygen abundances) of distant LIRGs which is compared to other galaxy samples. Discussion and conclusion are given in Sects. 7 and 8. Throughout this paper, a cosmological model with $H_0 = 70\ {\rm km\,s^{-1}\,Mpc^{-1}}$, $\Omega_{\rm M} = 0.3$ and $\Omega_{\Lambda} = 0.7$ has been adopted.

2. Sample selection, observations and data reduction

2.1. The fields

Our sample galaxies were selected from three ISO deep survey fields: CFRS $3^{\rm h}$, Ultra-Deep-Survey-Rosat (UDSR) and Ultra-Deep-Survey-FIRBACK (UDSF) fields.

The CFRS was carried out in five moderate to high galactic latitude ($|b| > 45°$) survey fields of area $10' \times 10'$ chosen to match the field of view of the MOS multiobject spectrograph on the 3.6 m CFHT. The $14^{\rm h}$ and $3^{\rm h}$ fields have been deeply imaged with the ISOCAM. Combining the deep IR observation and the deep optical and radio data, Flores et al. (1999) studied the 78 ISOCAM sources detected in the $14^{\rm h}$ field down to a 15 μm flux ≥250 μJy. In the CFRS $3^{\rm h}$ field, 70 sources were detected, with the 15 μm fluxes in the range of 170−2100 μJy (Flores et al. 2004a,b, in preparation).

The UDSR field refers to the Marano field (centered at $\alpha(2000) = 03^{\rm h}15^{\rm m}09^{\rm s}$, $\delta(2000) = -55°13'57''$), which is a deep ROSAT observation field. The deep (∼80 or 120 ks integration time) XMM-Newton observations (Giedke et al. 2001, 2003) and the optical identifications were also done (Lamer et al. 2003). FIRBACK is a deep survey conducted with the ISOPHOT instrument aboard the ISO at an effective wavelength of 175 μm. The total survey covers more than 4 square degrees located in one Southern and two Northern fields (Puget et al. 1999; Lagache & Dole 2001). For the UDSR and UDSF fields, very deep ISOCAM follow-up have been

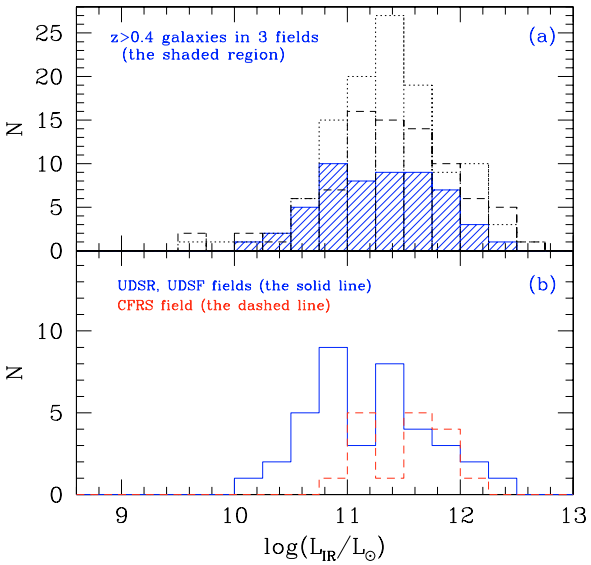

Fig. 1. a) The IR luminosity $\log(L_{\rm IR}/L_{\odot})$ distribution (bin = 0.25) of 55 ISO-detected sample galaxies with $z > 0.4$ in all of the three fields (the shaded region), with the median IR luminosity of $\log(L_{\rm IR}/L_{\odot}) = 11.32$, which is similar to those of the local IRAS sample of V95 and Kim et al. (1995) (the dotted-line for BGSs, and the dashed-line for WGSs, with the median values of 11.34 and 11.38, respectively). **b)** The distribution of the corresponding 38 galaxies with $z > 0.4$ in the UDSR and UDSF fields (the solid line), with the median IR luminosity of $\log(L_{\rm IR}/L_{\odot}) = 11.27$, and the distribution of the galaxies in the CFRS $3^{\rm h}$ field (the dashed-line), with the median IR luminosity of $\log(L_{\rm IR}/L_{\odot}) = 11.55$. Although the ISOCAM survey observations in the UDSR and UDSF fields are three times deeper than in the CFRS $3^{\rm h}$ field, the total distribution of the galaxies in the 3 fields is a reliable representation of the IR luminous galaxies in $z > 0.4$ Universe.

done (Elbaz et al. 2004) reaching flux limits three times lower than for the CFRS fields.

2.2. The sample

In the CFRS $3^{\rm h}$ field, we selected 25 targets out of the 70 ISO 15 μm sources according to their (α, δ) positions to observe by using VLT/FORS2. Another 9 objects without 15 μm fluxes were added to these observations to fill the FORS2 mask. In the UDSR field, 29 targets with ISO 15 μm fluxes were selected to be observed by using VLT/FORS2. Another 6 non-ISO objects were also added. Three slits (numbers 18, 19 and 25) were superposed on more than one object. In the UDSF field, 27 targets out of the ISO sources list were selected to be observed by using VLT/FORS2. Another 9 objects without 15 μm fluxes were also selected. Three slits (numbers 26, 27 and 29) were superposed on more than one object.

In total, 105 objects were selected for VLT/FORS2 spectral observations from the three fields. The basic data of the target galaxies are given in Tables 1 and 2. The columns are the slit numbers (also CFRS name in Table 1), the 2000 epoch coordinates, redshift z, I or R band photometric and spectral magnitudes in the AB system, aperture correction factor by comparing the photometric and spectral I or R band magnitudes, absolute B band magnitude M_B in the AB system, the spectral types of the objects, and the related infrared data including 15 μm fluxes, far-IR luminosities and IR-SFRs.

The IR luminosities (and deduced SFRs) have been calculated using the procedure given in Elbaz et al. (2002) and are given in Tables 1 and 2. They are based on mid-IR fluxes which show good correlations with radio and far-IR measurements in the local Universe (Elbaz et al. 2002). In the distant Universe, these estimates agree within a factor of 2 with those based on Hα luminosities (Flores et al. 2004a). Figure 1a shows the distribution (the shaded region) of the inferred IR luminosity (8−1000 μm) of the 55 ISO/15 μm-detected objects with $z > 0.4$ (the called "high-z" sample in the following parts of this paper) in the three fields for VLT/FORS2 spectroscopic observation (see Sect. 3 for redshifts) with a median value of $\log(L_{\rm IR}/L_{\odot}) = 11.32$. Figure 1b shows the corresponding distribution of the 38 $z > 0.4$ objects in the UDSR and UDSF fields with a median value of $\log(L_{\rm IR}/L_{\odot}) = 11.27$, and the distribution of the objects in the CFRS $3^{\rm h}$ field with a median value of 11.55. The difference is simply related to the different flux limits adopted in UDSR and UDSF fields on one side and on the CFRS $3^{\rm h}$ field, on the other side. However, our high-z sample exhibits IR luminosity distribution very similar to local IRAS galaxies studied by V95 and Kim et al. (1995), in which the median $\log(L_{\rm IR}/L_{\odot}) = 11.34$ for the Bright Galaxies (BGSs) and 11.38 for the Warm Galaxies (WGSs) (in Fig. 1a, the dotted-line for BGSs, and the dashed-line for WGSs). We believe that our sample can be used to probe the properties of distant LIRGs over an IR luminosity range comparable to that of V95.

2.3. Spectroscopic observations and data reduction

Spectrophotometric observations of the 105 targets were obtained during three nights with the ESO 8 m VLT using the FORS2 with $R600$, $I600$ at a resolution of 5 Å and covering the possible wavelength range between 5000 and 9200 Å. The slit width is 1.2″ and the slit length is 10″. Spectra were extracted and wavelength-calibrated using the IRAF[1] package. Flux calibration was done using 15 min exposures of 3 photometric standard stars per field. In addition, for one field (CFRS), we have compared the spectrophotometry to the V and I photometries and found a very good agreement. To ensure the reliability of the data, all spectrum extractions as well as lines measurements were performed by using the SPLOT program.

A rest-frame spectrum of one typical galaxy of our sample, UDSR23, is given in Fig. 2. The strong emission lines (e.g. [O II] λ3727, Hγ, Hβ, [O III] λ5007) and the obvious absorption lines are marked. The continuum has been convolved except at the locations of the marked emission lines using the softwares developed by our group (Hammer et al. 2001; Gruel 2002). The adopted convolution factors are 7 pixels and then 15 pixels.

[1] IRAF is distributed by the National Optical Astronomical Observatories, which is operated by the Association of Universities for Research in Astronomy, Inc., under cooperative agreement with the National Science Foundation.

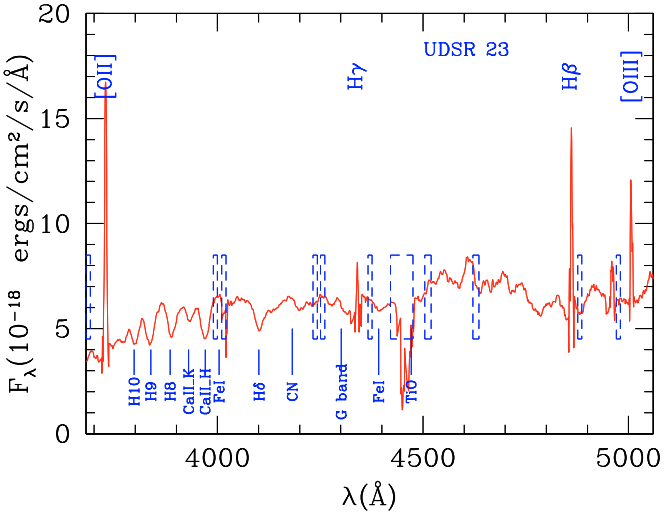

Fig. 2. Rest-frame spectrum of one of the sample galaxies, UDSR23. It is a luminous infrared galaxy with $\log(L_{\rm IR}/L_{\odot}) = 11.38$. The continuum has been convolved except at the location of the emission lines (e.g. [O II] λ3727, Hγ, Hβ and [O III] $\lambda\lambda$ 4959, 5007). The dashed boxes delimit the wavelength regions where strong sky emission lines (e.g. [O I]5577, 5891, 6300, 6364 Å and OH 6834, 6871, 7914 Å etc.) and absorption lines (O_2 6864, 7604 Å etc.) are located.

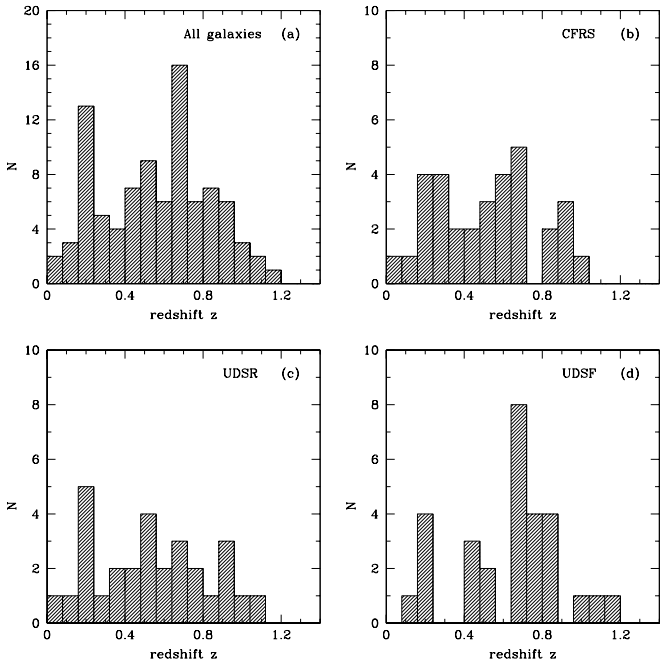

Fig. 3. Redshift distributions (bin=0.08) of the sample galaxies in the combined and the individual three fields.

3. Redshift distributions and spectral types

Redshifts are identified by using the emission and/or absorption lines. Column (4) of Tables 1 and 2 gives the z values of the objects. Redshift distributions of the combined and the individual three fields are shown in Fig. 3. The corresponding median redshifts are $z_{\rm med} = 0.587$ in the combined sample, $z_{\rm med} = 0.525$ in the CFRS, $z_{\rm med} = 0.521$ in the UDSR and $z_{\rm med} = 0.698$ in the UDSF. The redshift peak around $z = 0.70$ in the UDSF field (six galaxies) shows a velocity dispersion of ~1390 km s^{-1}, a typical value for a galactic cluster. The corresponding six objects are UDSF06, 07, 08, 21, 26a and 26b. In the UDSR field, four objects (UDSR11, 12, 13 and 16) show a redshift peak around $z = 0.166$, which may correspond to a velocity dispersion of ~129 km s^{-1}, a typical value for a galactic group.

The redshift distributions are consistent with the results in some other ISOCAM survey fields, e.g., the $z_{\rm med} = 0.7$ in the CFRS 14$^{\rm h}$ field (Flores et al. 1999) and 0.585 in the HDF-N (Aussel et al. 1999). Franceschini et al. (2003) found a peak at $z \sim 0.6$ for their 21 objects in the Hubble Deep Field South (HDF-S) field, which they suggested to be a cluster or a large galaxy concentration. The similarities between the IR luminosities as redshift distribution of our sample to those of other studies lead us to assume that our sample can be used to test the properties of distant LIRGs. About 81% (75/92) of the redshift-identified galaxies show obvious and strong emission line (EL) (see Col. 9 of Tables 1 and 2). The corresponding EL galaxies fraction of ISO-detected objects is ~85%. Table 3 summarizes the redshift identifications and spectral types of the galaxies in our sample.

4. Flux measurements, extinction and SFRs

4.1. Flux measurements

The fluxes of the emission lines are measured using the SPLOT package. The stellar absorption under the Balmer lines is estimated from the synthesized stellar spectra obtained using the stellar spectra of Jacoby et al. (1984). To do so, we use the spectra of four stellar types (e.g. A, B, F and G types) to synthesize the "galactic" continuum and absorption lines. Then, the "pure" emission Balmer lines are obtained through reducing the underlying stellar absorption. The corresponding error budget of emission line flux is deduced by a quadratic addition of three independent errors: the first one is related to the use of stellar templates to fit stellar absorption lines and continuum; the second one comes from the differences among independent measurements performed by Liang, Flores and Hammer; the third one is from the Poisson noises from both sky and objects, and it actually dominates the error budget. The flux measurements of emission lines and their percent errors are given in Table 4 for high-z galaxies, and in Table 5 for low-z galaxies. Three low-z galaxies are also given in Table 4 for their Hγ fluxes. To obtain reliable global fluxes of emission lines of the galaxies, we should notice that the 1.2″ slit of VLT observations does not always contain the whole galaxy. Thus, the fluxes of the emission lines are corrected by an aperture factor derived by comparing the photometric magnitudes to the spectral magnitudes at $I_{\rm AB}$ (for CFRS field) or $R_{\rm AB}$ (for UDSR and UDSF fields) bands. The aperture correction factors are given in Col. 7 of Tables 1 and 2.

4.2. Balmer decrement and extinction

The extinction inside the galaxy can be derived using the decrement between the two Balmer lines: Hγ/Hβ for our high-z galaxies, and Hα/Hβ for the low-z galaxies. Case B recombination with a density of 100 cm^{-3} and a temperature of 10 000 K was adopted, the predicted ratio is 0.466 for I_0(Hγ)/I_0(Hβ) and 2.87 for I_0(Hα)/I_0(Hβ) (Osterbrock 1989). Using the interstellar extinction law given by Fitzpatrick (1999) with R = 3.1 ($R = A(V)/E(B-V)$), the extinction can be readily determined. Using the Balmer decrement method we find a median extinction of A_V(Balmer) = 1.68 (=1.82 for the $z > 0.4$ sample). Extinction corrected Balmer lines (either Hβ or Hα) can be used to estimate the SFR, which could be then tested by comparison with SFR obtained from infrared flux.

4.3. Comparison between SFRs deduced from mid-IR and from Balmer lines

To compare the SFRs from IR and Balmer lines, we adopt the calibrations from Kennicutt (1998) based on the Salpeter's initial mass function (IMF) (Salpeter 1955) with lower and higher mass cutoffs of 0.1 and 100 $M_\odot$. The median SFR$_{\rm IR}$ of our sample galaxies is about 31 $M_\odot$ yr^{-1} for the $z > 0.4$ galaxies (it is 19 $M_\odot$ yr^{-1} when the low-z galaxies are included). The obtained median SFR$_{2.87f(\rm H\beta)}$ is about 28 $M_\odot$ yr^{-1} for $z > 0.4$ galaxies. For most galaxies, SFR$_{2.87f(\rm H\beta)}$ are consistent with SFRs estimated from infrared luminosities (Fig. 4a).

4.4. A robust estimate of the extinction coefficient

Because of the large uncertainties related to the measurements of the Hγ line, we need to verify the quality of our derived extinction. This can be done assuming that the infrared data provide a robust SFR estimate for IR-luminous galaxies (Elbaz et al. 2002; Flores et al. 2004a). We estimate a new dust extinction coefficient, A_V(IR), by comparing the infrared SFR with the SFR calculated from the optical Hβ emission line: the energy balance between IR and Hβ luminosities. Figure 4b shows that the derived A_V(IR) is consistent with A_V(Balmer) for most galaxies, most of them falling in the ±0.64 rms discrepancy. Few objects however lie outside the ±0.64 rms as shown in Fig. 4b (also see Table 6). For three of them (filled squares, CFRS10, CFRS19 and UDSF13) showing A_V(IR) much larger than A_V(Balmer), we believe that the discrepancy could be related to a possible overestimate of the IR flux due to contamination by neighboring ISO sources (the "possible flux blending" sources).

The derived median value of A_V(IR) is 2.18 (=2.36 for $z >$ 0.4 galaxies) for our sample, which is slightly larger than the extinction derived from optical Balmer lines. This trend might be related to the fact that infrared radiation includes fluxes from the optical thick H II regions, which might be obscured to contribute to the detected optical emission lines. An extreme example is CFRS25, CFRS03.0932, which shows A_V(Balmer) = 1.04 and A_V(IR) = 3.77. It is an extreme edge-on disk galaxy with an inclination of ~79° (Zheng et al. 2004). Most of the optical light of the whole galaxy is strongly hidden by dust (screen effect), and the detected optical Balmer lines just trace the star formation of a few optical-thin H II regions lying on the edge of the galaxy.

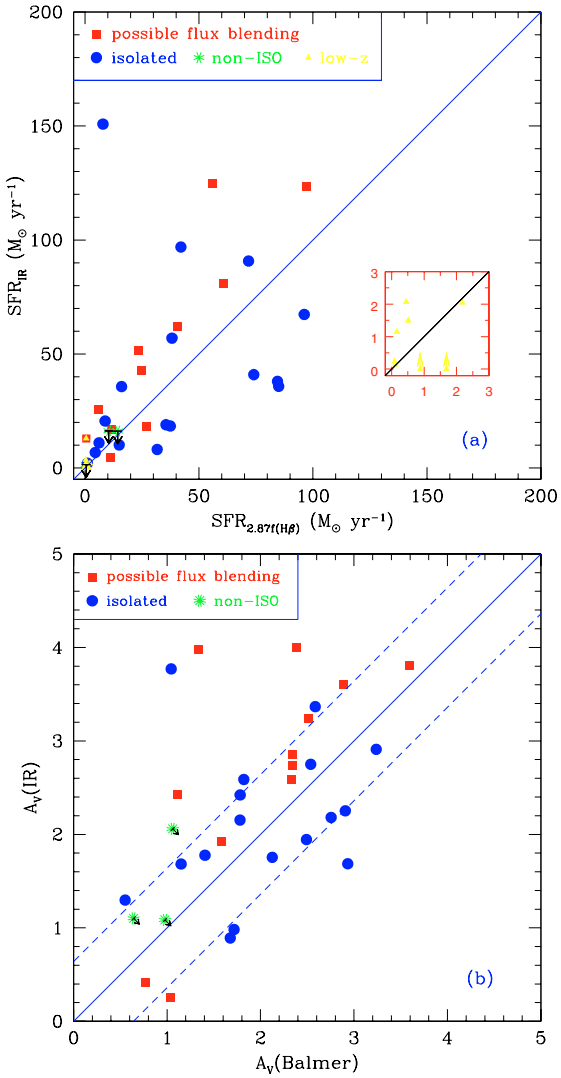

Fig. 4. a) The SFRs estimated from the extinction corrected Balmer lines (I_o(Hα) ≈ 2.87I_o(Hβ)) (also see Tables 6, 7), compared with the SFRs estimated from infrared fluxes. The small zoomed figure on the bottom right is for the low-z sample. Relative error bars (ΔSFR$_{\rm IR}$/SFR$_{\rm IR}$) are quoted in Tables 1 and 2, and average to 30% (see however a discussion by Cardiel et al. 2003). **b)** The relation between the extinction A_V values derived from Balmer decrement and by the energy balance between the IR radiation and the optical Hβ emission line luminosities. The two dashed lines refer to the results with ±0.64 rms. The different kinds of symbols in the two figures roughly show whether the infrared fluxes of the galaxies are affected by nearby objects according to their images from the VLT and the ISOCAM: the *filled squares* represent the objects for which the IR fluxes are possibly affected by other nearby ISO objects; the *filled circles* show the objects for which no contamination is expected; the *asterisks* mark the objects which are not detected by ISO, and their A_V(IR) are just upper limits.

The median extinction in our sample is lower than those of the local IRAS sample by V95 who obtained the median $E(B-V)$ (= A_V/3.1) values 0.99 for the H II LIRGs, and 1.14 for the

LINERs. This could be due to the fact that V95 only studied the central ~2 kpc parts of the IRAS galaxies, which could be more affected by dust than the whole galaxy light as studied in distant galaxies. The derived median extinction of our galaxies is comparable to that of radio-detected Sloan Digital Sky Survey (SDSS) galaxies ($A_{\rm H\alpha} = A_V/1.25 = 1.6$, Hopkins et al. 2003). It is much higher than those of the local normal star forming galaxies for which the median $A_V \approx 0.86$ (K92 and J20).

Comparison between the extinctions derived from IR and optical Balmer lines (Fig. 4b) provides a significant reduction of the error bars derived from the single Hβ/Hγ ratio, to ~0.64 for A_V. This might also provide a useful diagnostic for the dust and star formation properties in individual galaxies. In the following, we have to adopt a reliable A_V which describes as best as possible the global properties of each individual galaxy. The one based on the Hβ/Hγ ratio shows a large uncertainty because it is based on the faint Hγ emission line. Diagnostic diagrams and metal abundance determination often depend on the [O II] λ3727/Hβ ratio and then on the adopted extinction coefficient. It is uncertain whether such a ratio can be obtained as a global parameter for a given galaxy. On the other hand, using A_V(IR) could lead to overestimates of the extinction (and then to underestimates of the metal abundance) since it accounts for the most obscured regions. However the good correlation found by Flores et al. (2004a) between SFR$_{\rm IR}$ and SFR$_{\rm H\alpha}$ for LIRGs implies that strong obscuration are not preponderant in the energy balance for these galaxies. Because our study of the metal abundances is only based on starbursts and LIRGs (no ULIRGs), we adopt in the following A_V(IR) for estimating the extinction, while paying attention to how our results would be affected if using A_V(Balmer).

4.5. Continuum colors

The continuum colors of our sample galaxies are determined by the ratios of the continuum levels at 4861 Å and 3660 Å (C4861/C3660, for the high-z sample) and at 6563 Å and 4861 Å (C6563/C4861, for the low-z sample) (no extinction correction). We use the same three IR luminosity bins as V95 for $\log(L_{\rm IR}/L_\odot)$ ($\leq$11, between 11 and 12, and $\geq$12) in the following studies. Figure 5a shows the IR luminosity against the C4861/C3660 color for our sample galaxies. It seems that this plot shows that the more IR luminous galaxies with $\log(L_{\rm IR}/L_\odot) > 11$ have redder colors than the less luminous galaxies with $\log(L_{\rm IR}/L_\odot) \leq 11$. However, the trend is very weak(less than 1σ) and similar to the result of V95 (their Fig. 17, for C6563/C4861 vs. IR luminosity). Figure 5b shows the color excess (extinction) against the C4861/C3660 color for our sample. It shows a weak positive correlation, i.e., the redder color, the higher dust extinction, which is similar to that of the local IRAS sample shown by Fig. 5 of V95 (with C6563/C4861 color). Figure 5c shows the color excess against the C6563/C4861 color for the low-z sample. It seems that a weak correlation exists as well, similar to that of V95 (on their Fig. 5). The median color C6563/C4861 value is about 0.4. If the dust extinction is considered to correct the continuum color roughly, the median color $(\rm C6563/C4861)_0$

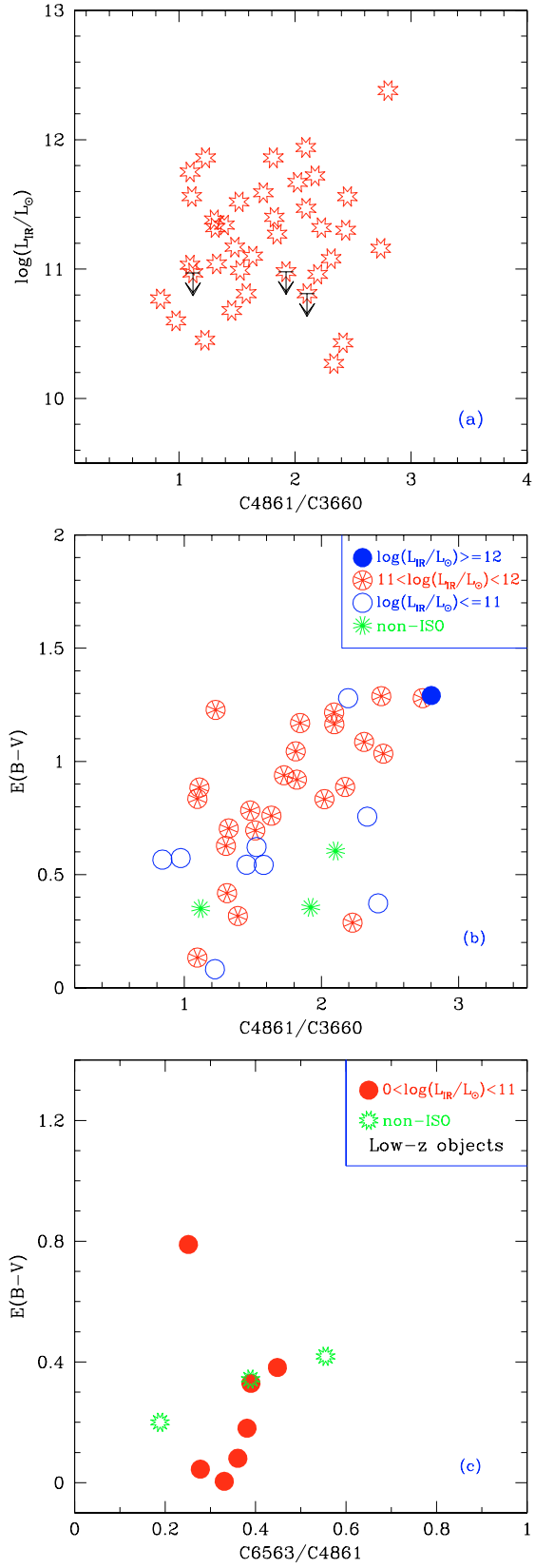

Fig. 5. The far-IR luminosities and color excesses (extinction) as functions of continuum colors for our sample galaxies: **a)** IR luminosities, **b)** extinction for the high-z sample, **c)** extinction for the low-z sample. The continuum colors are defined as the ratios of the continuum levels close to the lines (no extinction correction) (on both sides ~4 Å around the line), with a typical uncertainty 0.03.

("0" means extinction correction) is about 0.35, which is similar to the value 0.4 obtained by V95 for their local IRAS sample (their Fig. 16).

5. Diagnostic diagrams

5.1. High redshift galaxies

The diagram of log([O II] λ3727/Hβ) vs. log([O III] $\lambda\lambda$4959, 5007/Hβ) can be used to distinguish the H II region-like objects from the LINERs and Seyferts. The H II region-like objects can be H II region in external galaxies, starbursts, or H II region galaxies, objects known to be photoionized by OB stars.

Figure 6a gives the diagnostic diagram for our $z > 0.4$ galaxies, and shows that most of the objects are H II region galaxies, and are consistent with the theoretical fitting of the local extragalactic H II regions (the solid line, from McCall et al. 1985). The dashed line shows the photoionization limit for a stellar temperature of 60 000 K and empirically delimits the Seyfert 2 area from the H II region area (also see Hammer et al. 1997). From this plot, eight objects are identified to be AGNs, including five LINERs (CFRS17, 32, 33, UDSR04 and UDSF32) and three Seyfert 2 galaxies (UDSR09, UDSF13, 28). An AGN fraction of ~23% is identified from the diagnostic diagram. However, this ratio can be decreased to 11% when A_V(Balmer) instead of A_V(IR) is used to correct the emission line fluxes. One reason for this is the higher extinction of A_V(IR) results in higher [O II] emission line flux corrected by extinction, hence, a higher LINER fraction. The AGN fraction is consistent with previously reported results (17%, Fadda et al. 2002).

5.2. Low redshift galaxies

For the low-z galaxies, the diagnostic diagrams of [O III] λ5007/Hα vs. [S II] $\lambda\lambda$6716, 6731/Hα and [O III] λ5007/Hα vs. [N II] λ6583/Hα are available to diagnose their source of ionization (Veilleux & Osterbrock 1987; Osterbrock 1989). Figures 6b and c show these properties of the sample galaxies.

From the [S II]/Hα vs. [O III]/Hβ relations, most of the galaxies are LINERs with low ionization levels. However, from the [N II]/Hα vs. [O III]/Hβ relations, most of the galaxies are H II region galaxies since only two objects (20%) show the LINER character (UDSR06, 11). Also, most of them will be classified to be "Star Forming" galaxies by using the corresponding diagnostic for the SDSS sample (Kauffmann et al. 2003; Brinchmann et al. 2003). Thus, to study the diagnostic diagrams of such emission line galaxies, these two diagrams are needed simultaneously (also see Liang et al. 2004). Considering the limits given by Kewley et al. (2001) (the long-dashed lines in Figs. 6b and c), most of the low-z galaxies would be classified as H II regions. It may infer that most of them occupy a region intermediate between LINERs and H II regions.

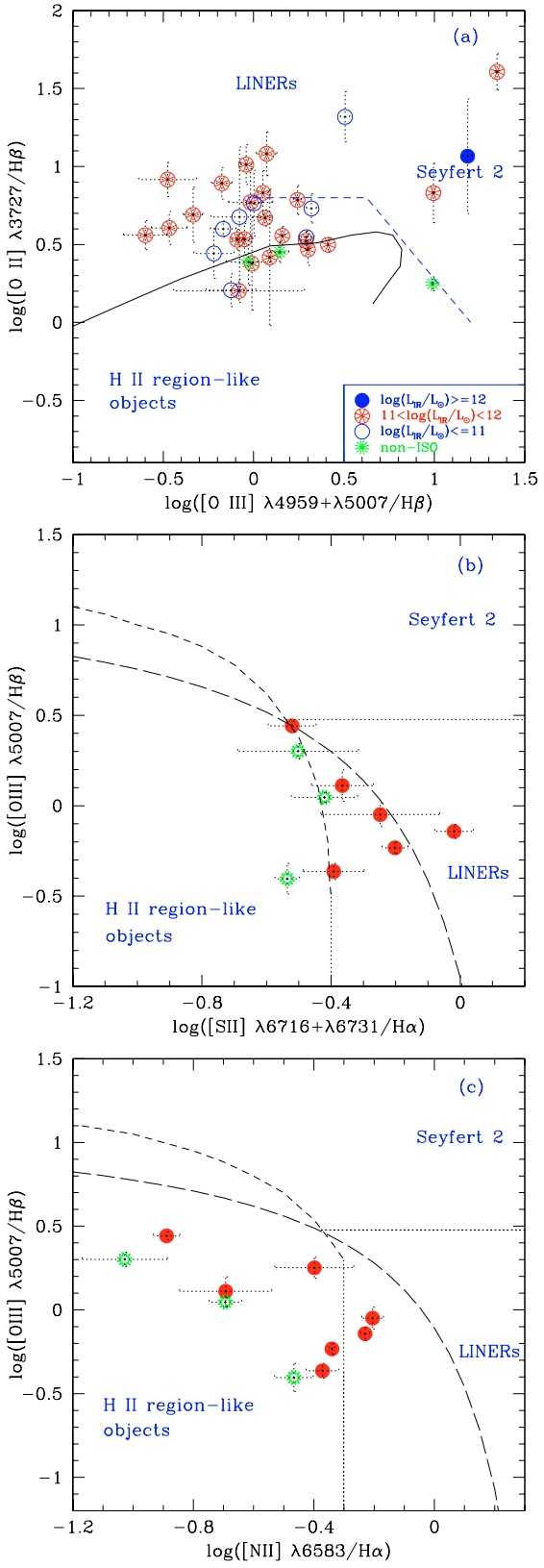

Fig. 6. a) Diagnostic diagram for our high-z sample. The solid line shows the theoretical sequence from McCall et al. (1985), which fits the local extragalactic H II regions well with metallicity decreasing from left to right. **b), c)** Diagnostic diagrams for the low-z sample, with symbols as in Fig. 5, and the long-dashed lines are taken from Kewley et al. (2001), others are from Osterbrock (1989).

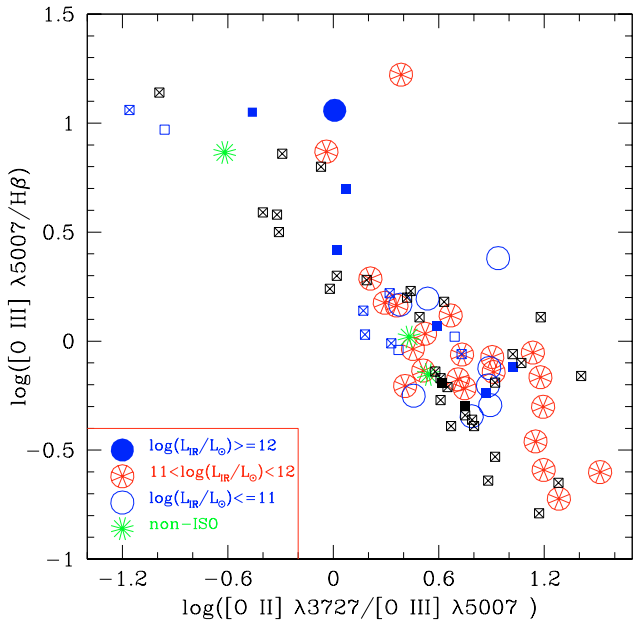

Fig. 7. [O III]λ5007/Hβ versus [O II]λ3727/[O III]λ5007 emission line flux ratios of our sample galaxies, compared with the local IRAS sample from V95. The typical (median) uncertainties of the two parameters in logarithm are 0.08 and 0.12 dex, respectively. The *squares* are the IRAS data: the *open squares* represent the galaxies with $\log(L_{\rm IR}/L_\odot) < 11$, the *squares with a cross in the middle* are the galaxies with $11 \le \log(L_{\rm IR}/L_\odot) \le 12$, and the *filled squares* are the galaxies with $\log(L_{\rm IR}/L_\odot) > 12$. Most of our sample galaxies have relatively low ionization levels ([O III]/Hβ < 3).

5.3. [O III]/Hβ versus [O II]/[O III] diagram for high-z galaxies

The ([O II] λ3727/[O III] λ5007) emission line ratio follows a sequence from low-excitation H II regions to high-excitation H II regions (Baldwin et al. 1981). Figure 7 shows the log([O III] λ5007/Hβ) vs. log([O II] λ3727/[O III] λ5007) diagnostic relation for our sample, compared with that for local IRAS LIRGs of V95. Most of our galaxies lie in the bottom right region indicating low ionization levels ([O III]/Hβ < 3). The apparent excess of high ionization objects in V95 could be attributed to the fact that they only studied the central ∼2 kpc of the IRAS galaxies, and that they could be more sensitive to a possible high ionization central AGN. Another possible selection bias in V95 might also contribute to this excess, since they have been able to detect [O II] λ3727 line only in their brightest and more distant sources, which likely include more objects with high ionization levels.

6. Abundances in interstellar medium and luminosity–metallicity relation

Chemical properties of gas and stars within a galaxy are like a fossil record chronicling its history of star formation and its present evolutionary status. The high quality optical spectra from VLT/FORS2 make it possible, for the first time, to obtain the chemical abundances in ISM for such a large sample of high-z LIRGs.

6.1. Metallicities estimated from diagnostic diagram

On the diagnostic diagram of log([O II] λ3727/Hβ) vs. log([O III] $\lambda\lambda$4959, 5007/Hβ), the local H II region samples with different metallicities lie in different areas. Moreover, they follow the empirical sequence from McCall et al. (1985), which fits the local H II galaxies well with metallicity decreasing from the left to the right (see Fig. 12 of Hammer et al. 1997). The corresponding relations for our galaxies are given in Fig. 8a (the larger points), together with the local H II regions with different metallicities (the smaller points, the representative metallicities of the different symbols are shown in the box on the bottom right, Z_0 is the solar metallicity). The solid line shows the theoretical sequence from McCall et al. (1985). This diagram shows that our high-z H II region galaxies fall in the local sample well, and have metallicities of $0.5\,Z_\odot < Z < Z_\odot$. One non-ISO galaxy, UDSF26a, perhaps has low metallicity with $Z < 0.25\,Z_\odot$. It seems that there is no obvious difference in metallicities between the more luminous infrared H II galaxies ($\log(L_{\rm IR}/L_\odot) > 11$) and other less luminous infrared samples ($\log(L_{\rm IR}/L_\odot) \le 11$).

This plot shows that the horizontal-axis parameter, log([O III] $\lambda\lambda$4959, 5007/Hβ), can trace the metallicities of the H II galaxies roughly, following a trend that increasing values (up to ∼1.0) corresponds to lower metal abundances. Also, this ratio is almost independent of extinction. Therefore, we further obtain the $\log(L_{\rm IR}/L_\odot)$ vs. log([O III] $\lambda\lambda$4959, 5007/Hβ) (no extinction correction) relation shown by Fig. 8b, in which more data points are included though their Hγ emission lines (for extinction) and/or [O II] λ3727 shift out of the rest-frame spectra. Figure 8b indicates that there is almost no obvious correlation between the two parameters, if one exists, a very weak correlation may show the decreasing [O III]/Hβ ratio following the increasing IR luminosity for the high-z galaxies when the three Seyfert 2 galaxies (with log([O III] $\lambda\lambda$4959, 5007/Hβ) > 1.0) are excluded.

6.2. Oxygen abundances estimated from strong emission lines

The "direct" method to determine chemical compositions requires the electron temperature and the density of the emitting gas (Osterbrock 1989). In a best-case scenario, the electron temperature of the ionized medium can be derived from the ratio of a higher excitation auroral line, such as [O III] λ4363 to [O III] $\lambda\lambda$4959, 5007. However, [O III] λ4363 is too weak to be measured except in extreme metal-poor galaxies, and becomes extremely weak in more metal-rich environments due to abundant heavy elements reducing collision excitation of the upper levels. In this case, the oxygen abundances may be determined from the ratio of [O II]+[O III] to Hβ lines ("strong line" method). The general parameter is R_{23}: R_{23} = ([O II]λ3727 + [O III]λ4959 + [O III]λ5007)/Hβ.

Many researchers have developed formula for converting R_{23} into oxygen abundance. The different calibrations have been checked by Kobulnicky & Zaritsky (1999) and Kewley & Dopita (2002). Recently, using the calibration given by McGaugh (1991), Kobulnicky et al. (1999) presented two

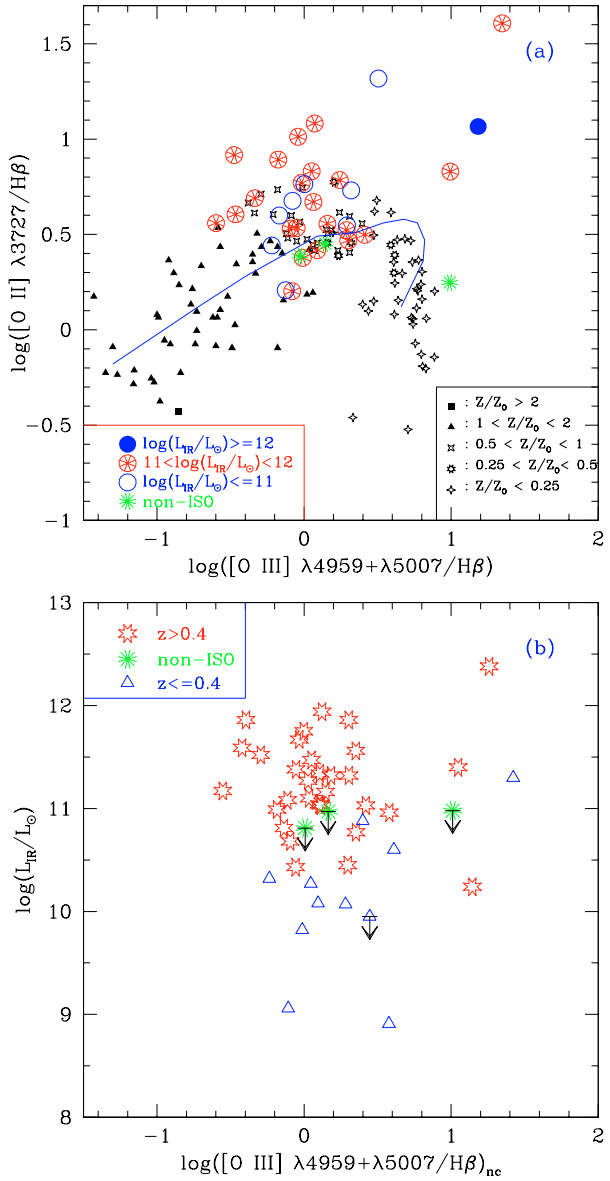

Fig. 8. **a)** The relation between log([O II] λ3727/Hβ) and log([O III] $\lambda\lambda$4959, 5007/Hβ) for $z > 0.4$ galaxies, compared with a sample of local H II regions and H II galaxies with different metallicities (see Fig. 12 of Hammer et al. 1997 for references of H II samples). The solid line shows the theoretical sequence from McCall et al. (1985), same as in Fig. 6a. **b)** The relation between the infrared luminosities and the log([O III] $\lambda\lambda$4959, 5007/Hβ) (not corrected by extinction), which includes more data points than figure **a)** panel since some galaxies can be added according to their [O III] to Hβ ratios which are almost independent of extinction.

analytic formulae to convert R_{23} into 12+log(O/H) for the metal-rich and metal-poor branches, respectively. Here we only adopt the calibration for the metal-rich branch since the related sample includes only luminous galaxies ($M_B < -18$) (Kobulnicky et al. 1999):

$$\begin{aligned} 12 + \log(\mathrm{O/H}) =& 12 - 2.939 - 0.2x - 0.237x^2 - 0.305x^3 \\ & -0.0283x^4 - y\big(0.0047 - 0.0221x \\ & -0.102x^2 - 0.0817x^3 - 0.00717x^4\big), \end{aligned} \quad (1)$$

where x refers to logR_{23}, and y refers to logO_{32}: log(O_{32}) = log(([O III]λ4959 + [O III]λ5007)/[O II]λ3727). To translate R_{23} to be 12+log(O/H), the different calibrations will cause slightly different oxygen abundances. In fact, it is not important which calibration is used here since we are interested in the relative abundances between local and distant galaxy samples analyzed in the same manner. For the comparison samples in Fig. 9 (K92; J20; Kobulnicky et al. 2003; Lilly et al. 2003), the same calibration (Kobulnicky et al. 1999) has been adopted.

Due to the limits of wavelength ranges, [O II]λ3727 emission lines shift out of the visible wavelength in the low-z galaxies. Oxygen abundances in ISM of these galaxies can be estimated by R_3 parameter for this case (Edmunds & Pagel 1984): $R_3 = 1.35 \times$ ([O III]λ5007/Hβ). Then, their 12 + log(O/H) values can be obtained using the empirical relation proposed by Vacca & Conti (1992) (also see Coziol et al. 2001):

$$\log(\mathrm{O/H}) = -0.69 \times \log R_3 - 3.24, \quad (-0.6 \le \log R_3 \le 1.0).$$

The derived 12 + log(O/H) values of the galaxies are given in Col. 12 of Table 6 (for high-z sample) and Col. 8 of Table 7 (for low-z sample), which show that our high-z H II region galaxies have 12 + log(O/H) from 8.36 to 8.93, with a median value of 8.67. Two low-z galaxies have higher metallicities than 9.0. We should notice that here and hereafter the mentioned "oxygen abundance" or "metallicity" refers to "gas-phase" value in the ISM.

For the solar metallicity, Anders & Grevesse (1989) obtained a value of 12 + log(O/H) = 8.90, Grevesse & Sauval (1998) got 8.83, whereas Allende Prieto et al. (2001) gave a preferred solar value of 8.68. Therefore, in the following, our discussion is based wherever possible on 12 + log(O/H) values rather than metallicities relative to solar, in order to avoid confusion.

6.3. Luminosity-metallicity relation

In the local Universe, metallicity is well correlated with the absolute luminosity of galaxies (Zaritsky et al. 1994; Contini et al. 2002; Melbourne & Salzer 2002; Lamareille et al. 2004). Based on the current understanding of cosmic evolution, the volume-averaged star formation rate was higher in the past (Madau et al. 1996; Lilly et al. 1996; Flores et al. 1999) and the overall metallicity in the Universe at earlier times was correspondingly lower. We might expect galaxies to be considerably brighter at a given metallicity (i.e. luminosity evolution) if they are forming stars at higher rates. A high or intermediate redshift galaxy sample ought to be systematically displaced from the local sample in the L–Z plane if individual galaxies reflect these cosmic evolution processes. However, if local effects such as the gravitational potential and "feedback" from stellar winds and supernova regulate the star formation and chemical enrichment process, the L–Z relation might be less dependent on the cosmic epoch. In fact, feedback could confuse the use of metallicity as a simple metric (Garnett 2002).

Figure 9 presents the M_B vs. 12 + log(O/H) relations for our LIRG sample, compared with the local (from K92 and J20) and the other two high-z samples (from Kobulnicky et al. 2003 and Lilly et al. 2003). The M_B values of the compared samples

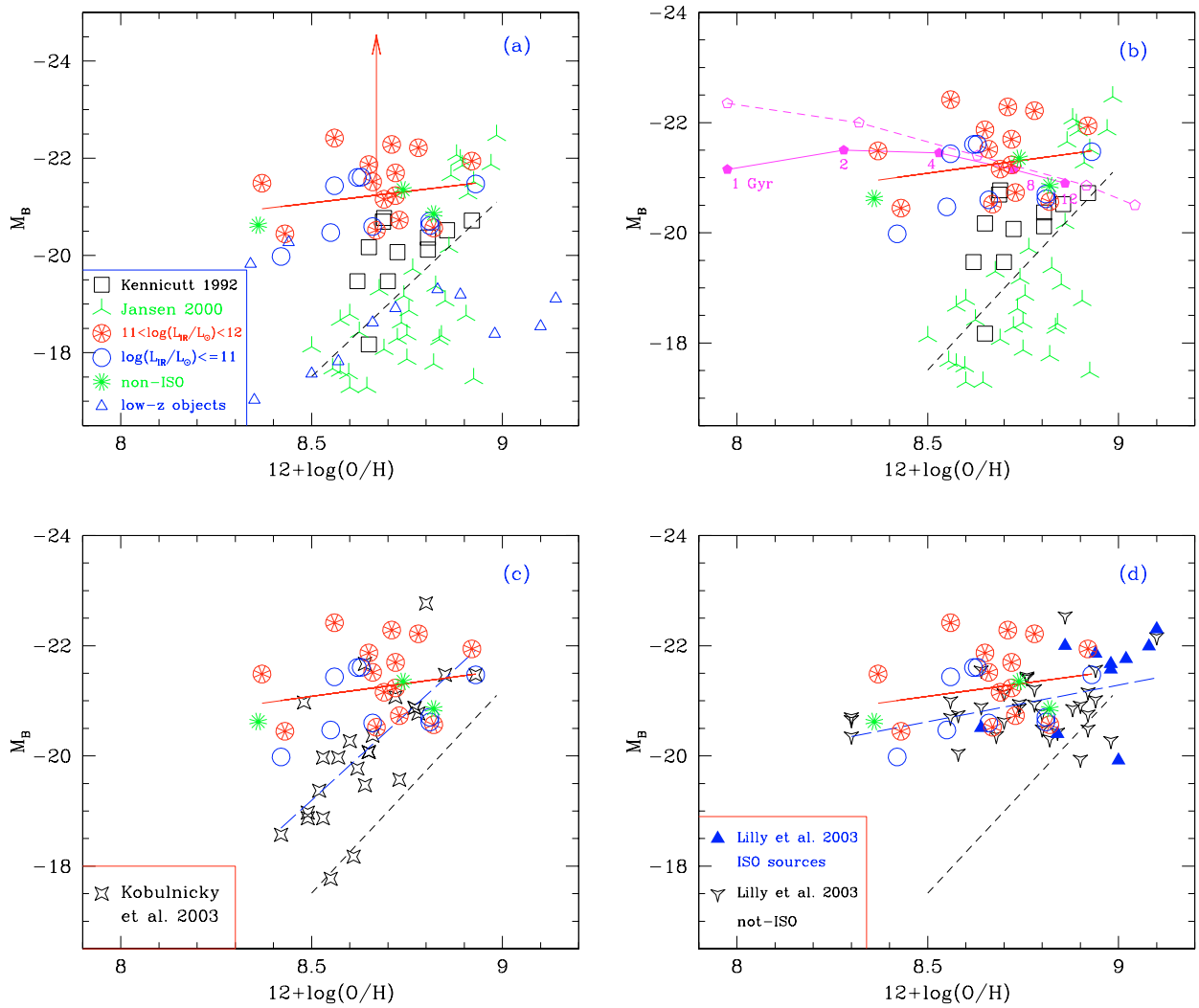

Fig. 9. The M_B−metallicity relation of our distant LIRGs (with the typical uncertainty of 0.08 dex on metallicity), compared with other samples and Pegase2 models: **a)** with the local galaxies from K92 and J20; the vertical arrow connecting with the solid fit line shows the maximal extinction effect on M_B, assuming an average extinction correction of $A_V = 2.36$. **b)** Pegase2 infall models are superimposed assuming a total mass of 10^{11} $M_\odot$ and infall times of 5 Gyr and 1 Gyr (the solid and dashed lines with pentagons, respectively); the different timescales are indicated below pentagons. **c)** With the galaxies with $0.4 < z < 0.82$ from Kobulnicky et al. (2003). **d)** With the galaxies with $0.47 < z < 0.92$ from Lilly et al. (2003); solid triangles represent the LIRGs in the Lilly et al. sample for which we suspect that their location should move to lower metal abundance values (see text), reconciling their results to ours and those of Kobulnicky et al. The linear least-squares fits of the samples are given: the *solid line* is for our distant LIRGs, the *short-dashed line* for the local sample, and the *long-dashed lines* for the other two high-z samples.

have been corrected to be the same cosmological model as ours and in the AB system. The linear least-squares fits for the corresponding galaxy samples are also given by considering the metallicity as an independent variable.

6.3.1. Comparison with local disks

Figure 9a compares the L–Z relation for the LIRGs to that of local disks (K92 and J20), which are restricted to moderately star forming galaxies ($EW(\mathrm{H}\beta) < 20$ Å) following Kobulnicky et al. (2003). For the local disks, there is a correlation between L_B and Z, with some dispersion at low luminosity, which could be related to different star formation histories at different epochs. For the brightest/more abundant disks, this might be translated into a mass-abundance relation, assuming that their B lights are dominated by emissions from intermediate or old stellar populations. Most of the low redshift sample galaxies (the *triangles*) lie in the disk locus, which could be simply related to the fact that they show moderate SFRs, and are not so different from the local disks. Two of the low-z galaxies (CFRS09, 13) show high metal abundances 12 + log(O/H) > 9.0). They are the so-called "CFRS Hα-single" galaxies studied by Liang et al. (2004), and are over-abundant spirals. The situation for distant LIRGs is far more complex. At a given metal abundance, all of them show much larger B luminosities than local disks, which corresponds to $\delta M_B = 2.5$ mag at the median 12+log(O/H) = 8.67 (with the median $M_B = -21.24$). These galaxies show ∼0.3 dex lower

metallicity than that of the local disks with the similar B luminosity (e.g. the median $M_B = -21.24$). Adopting A_V(Balmer) instead of A_V(IR) would move the median metal abundance value of our galxies by +0.03 dex.

The small M_B variation with metallicity is probably related to selection effect because distant ISOCAM sources likely correspond to luminous (and massive?) systems (also see Franceschini et al. 2003). As an aside, they are also consistent with an infall model (single-zone Pegase2 from Fioc & Rocca-Volmerange 1999) as displayed in Fig. 11 of Kobulnicky et al. (2003) for a 10^{11} $M_\odot$ galaxy (our Fig. 9b). The model assumes a SFR proportional to the gas mass where the galaxy is built by exponentially decreasing infall of primordial gas with an infall timescale of 5 Gyr (the solid line with pentagons). Here the nucleosynthesis yields of stars (from the B-series models of Woosley & Weaver 1995) have been arbitrarily reduced by a factor of 2 to avoid overproduction of metals at late times (see Kobulnicky et al. 2003). The dispersion of the points around this relation may be reproduced by adding singular burst of star formation of 10^{6-7} $M_\odot$ on the model galaxy.

However, we believe that Fig. 9a does not tell us all of the story. Indeed, distant LIRGs show SFRs extending from 30 to several hundreds of $M_\odot\,\mathrm{yr}^{-1}$ and high gas extinctions. Conversely to local quiescent disks, their B luminosities are dominated by young stars, and as such, are strongly affected by dust effects. The latter cannot be accurately estimated from their spectral energy distribution, without a careful modelling of stellar populations, IMF and of the dust geometry. We can estimate the maximal B luminosity of distant LIRGs, which can be reached if all blue stars were embedded in the ionized gas. This "maximal" dust correction is represented in Fig. 9a by a big vertical arrow connecting with the linear least-squares fit of our high-z LIRGs sample, assuming an average extinction correction A_V(IR) = 2.36 (or 3 mag at 4350 Å). Then, at a given metal abundance, LIRGs have B luminosities by far larger than those of the local disks, which excess δM_B ranging from 2.5 mag to more than 5 mag at the median 12 + log(O/H) = 8.67. Assuming an infall gas model, distant LIRGs could be interpreted as forming very massive systems with total mass ranging from 10^{11} $M_\odot$ to $\leq 10^{12}$ $M_\odot$, which extend from massive disks to massive ellipticals.

It is valuable to notice that, at the given magnitude (the median value), the metallicity of the distant LIRGs are also lower by ~0.3 dex than those of other local samples (Contini et al. 2002; Lamareille et al. 2004; Melbourne & Salzer 2002). Because the above studies are based on UV or Hα emission, they mostly include low luminosity (mass?) systems in the local Universe. In Fig. 9a we have chosen to compare our results to those of more massive objects, i.e. the spiral galaxies from K92 and J20, because this provides us a better tool to understand evolutionary effects.

6.3.2. Comparison with other high-z samples

Figure 9c compares the distant LIRGs with the high-z galaxies from Kobulnicky et al. (2003) with $0.4 < z < 0.82$ (EW(Hβ) < 20 Å). Kobulnicky et al. estimated the O/H values using R_{23} and O_{32} parameters obtained from the corresponding equivalent widths of the lines, which are believed to be less affected by dust extinction (see Kobulnicky & Phillips 2003). The metallicities of their galaxies are in similar range to ours, but the galaxies are fainter at a given metallicity. The median (M_B, 12 + log(O/H)) of their sample is about (8.64, −20.08). The difference between the two samples decreases at increasing metallicity, from δM_B = 2.3 mag at 12 + log(O/H) ~ 8.42 to δM_B = 0 at 12 + log(O/H) ~ 8.85. The δM_B is ~1 mag at the median abundance of 8.67 of our LIRGs. This discrepancy in M_B reflects that our sample galaxies are brighter and possibly more massive than the rest-frame blue selected sample of DGSS galaxies.

Figure 9d compares the distant LIRGs with the distant CFRS sample studied by Lilly et al. (2003). The M_B values of the two galaxy samples are very similar, from about −19.8 to −22.5. The linear least-squares fits of the two samples (the solid line is for our sample, and the long-dashed line is for Lilly's sample) show a non-significant difference in L–Z relation: $\delta M_B \sim 0.4$ mag. For reasons of clarity, we have restricted the sample of Lilly et al. (2003) to the CFRS 3^h and 14^h fields, which have been surveyed by ISOCAM. Among this subsample of 42 galaxies, 10 have been identified to be LIRGs by ISO (shown as *filled triangles* in Fig. 9d). The derived oxygen abundances by Lilly et al. for these 10 ISO-galaxies show a median value of 12 + log(O/H) = 8.98, which is ~0.3 dex higher than the median value of our distant LIRG sample. Indeed, Lilly et al. (2003) assumed a constant extinction of $A_V = 1$ for all their galaxies, which strongly underestimates the average extinction for LIRGs, and then, leads to underestimated [O II]λ3727/$H\beta$ ratios, hence the overestimated oxygen abundances. This effect has been checked by us in investigating the properties of two common galaxies in the two samples. For CFRS02 (A_V = 3.24) and CFRS06 (A_V = 2.74), Lilly et al. (2003) found the 0.5 dex and 0.3 dex larger 12 + log(O/H) values than our estimates, respectively. If one assumes an average A_V = 2.36 for LIRGs in the Lilly et al. sample, this would move all the corresponding points (full triangles) towards a lower metallicity by ~0.3 dex. Extinction effects could thus reconcile Lilly et al.'s results with those of Kobulnicky et al. (2003).

7. Discussion

We have gathered a sample of 105 ISOCAM galaxies for which we present detailed optical spectroscopic properties. The sample, although slightly biased towards high IR luminosity, shows several strikingly similar properties with the local sample of IRAS galaxies studied by V95 and Kim et al. (1995). This includes a similar IR luminosity distribution, continuum color, extinction and ionizing properties. We believe that our sample provides a good representation of distant LIRG properties. We also confirm that, for >77% of the distant LIRGs selected by ISOCAM at 15 μm, star formation is responsible for most of their IR emission.

ISO distant galaxies present a L–Z diagram strikingly different from that of local disks. Distant LIRGs are forming stars at very large rates, and their L–Z diagram is almost an

horizontal line reaching the local disk L–Z correlation: they are the systems actively building up their metal content. At the median luminosity ($M_B = -21.24$), their median $12+\log(O/H)$ is about 0.3 dex smaller than the local disk value, and even less if we correct the M_B value for extinction. It is unlikely that this discrepancy is related to our determination of metallicity, because we have adopted the conservative assumption that all distant LIRGs lie on the upper branch of the R_{23} − O/H diagram, i.e. with $12 + \log(O/H) \geq 8.35$. In the following, we investigate the relation between distant LIRGs and present-day disk galaxies.

LIRGs can reach the local disk locus by either a progressive enrichment of their metal content or fading. Both cases are somewhat extreme. Single-zone infall models with infall time from $\tau = 1$ to 5 Gyr could easily reproduce the link between distant LIRGs, the distant large disks, and the local massive disks (see Fig. 9b). These models predict the total masses of galaxies range from $10^{11}\ M_\odot$ to $\leq 10^{12}\ M_\odot$. The latter mass value comes from the maximal B band luminosity (see Sect. 6.3.1). As noticed by Kobulnicky et al. (2003), reducing the infall time (to values down to few 10^8 years) would lead to overproduction of metal at later times. However, we believe that simple infall models cannot apply during the whole history of the galaxy: several factors can prevent the star formation from being held at very large rates, including disk self regulation (Silk 1997), gas consumption or small timescales related to merging events.

A major problem is the uncertainty about the characteristic infall time: if much smaller than 1 Gyr, distant LIRGs might fade away after the burst and be progenitors of low mass disks. It is likely that LIRGs correspond to specific events of strong star formation in galaxy history: if associated to mergers, such events should be rather short, within few 10^7 to 10^8 years, leading to relatively small amounts of formed stellar mass and metals. Indeed, several consecutive bursts are predicted by merging simulations. Several minor merger events may occur in a Hubble time. The study of the Balmer absorption lines of these LIRGs will be presented in a forthcoming paper (Marcillac et al. 2004), in which they will be used to quantify the mass fraction of stars born during the starbursts as well as the duration of these bursts.

LIRG morphologies suggest that a noticeable amount of them are intimately linked with the population of large disks. Using HST color maps of 34 distant LIRGs drawn from the CFRS sample, Zheng et al. (2004) showed that 36% of the LIRGs have disk morphologies and only 17% are major mergers of two galactic disks, which confirms the preliminary study in Flores et al. (1999). Lilly et al. (1998) have gathered a small but representative sample of large disks ($r_{\rm disk} \geq 4\ h_{50}^{-1}$) at $z \geq 0.5$, which appears in number density comparable to that of local large disks. Restricting this sample to the two CFRS fields surveyed by ISO ($3^{\rm h}$ and $14^{\rm h}$), 6 (30%) of the 19 large disks are LIRGs ($L_{\rm IR}$ from 3 to $18 \times 10^{11}\ L_\odot$) detected by ISO (4 of them are indeed detected by ISO but 2 of them are in the supplementary catalog of Flores et al. 1999; also see Zheng et al. 2004). If we assume that the sample of Lilly et al. (1998) is a good representation of massive disks in the $0.5 < z < 1$ volume, and that a large fraction of them are experiencing strong star forming episodes (LIRGs), this could constraint the amount of metal/stellar mass they have formed. The elapsed time between $z = 1$ and $z = 0.5$ is ∼2.7 Gyr, and if 30% of distant disks are experiencing strong star formation episodes (LIRGs), infall time likely averages to a value close to 1 Gyr: this would suffice to produce an amount of metal to reach the upper metal branch of local massive disks.

Unfortunately, at present, we only have a few K band measurements for the sample galaxies studied here to estimate their stellar masses. However, Zheng et al. (2004) has derived rest-frame K-band luminosities ranging from $1.4 \times 10^{10}\ L_\odot$ to $2.9 \times 10^{11}\ L_\odot$ for 24 of their distant LIRGs. The characteristic time for doubling the stellar masses of the distant LIRGs ranges from 10^8 to 10^9 years. Since in the very simple model (1 Gyr infall) described above, a noticeable fraction of the gas was not converted into stars, this supports our view that LIRGs are related to the formation of massive systems (∼$10^{11}\ M_\odot$, mostly large disks). On average, $z \sim 1$ large disks could double their metal content and their stellar mass to reach the massive spiral locus at $z < 0.5$. This is consistent with Franceschini et al. (2003), who found that the distant IR sources in the HDF-S are hosted by massive galaxies ($M \sim 10^{11}\ M_\odot$), with an observed median star forming activity parameter, $M/SFR \sim 1$ Gyr.

Our result is globally in agreement with that of Franceschini et al. (2003) who found that the host galaxies of ISO sources are massive members of groups with typically high rates of star formation ($SFR \sim 10$ to $300\ M_\odot\,{\rm yr}^{-1}$), and suggested that the faint ISOCAM galaxies appear to form a composite population, including moderately active but very massive spiral-like galaxies, and very luminous ongoing starbursts, in a continuous sequence.

8. Conclusion

A large sample (105) ISO/15 μm-selected sources in three ISO deep survey fields (CFRS $3^{\rm h}$, UDSR and UDSF) are studied on the basis of their high quality VLT/FORS2 spectra and the infrared data from ISO. Among the 92 redshift-identified objects, 75 (64 with $z > 0.4$) are classified to be EL galaxies. 66 (55 with $z > 0.4$) objects are EL galaxies out of the 77 ISOCAM 15 μm detected sources. This is by far the largest sample of spectra of distant ISO galaxies. We present here their properties derived from the emission lines. The redshift distribution ($z_{\rm med} = 0.587$) is consistent with that of previous studies, and some galaxies belong to a $z \sim 0.70$ cluster (in the UDFS field) or to a $z \sim 0.166$ galaxy group (in the UDSR field). This study provides us:

- An accurate calculation of the extinction coefficient from Balmer emission lines, which properly account for underlying Balmer absorption (A_V(Balmer), median value of 1.82 for $z > 0.4$ sample galaxies).
- An energy balance between IR and Balmer luminosities which provides us with an original way to calculate an IR-based extinction coefficient (A_V(IR), median value of 2.36 for $z > 0.4$ galaxies).
- A good correlation between the above-mentioned two extinction coefficients, which, for the first time, allows us to

reliably obtain the chemical properties of distant galaxies with considering interstellar extinction; this diagram could also be used as a diagnostic of their dust geometry and star formation history.
- The very similar general properties of $z > 0.4$ ISO sources to those of the local IRAS LIRGs studied by V95, including IR luminosity distribution, continuum color, ionization and extinction properties, which ensures that our sample is representative of LIRGs in the distant Universe.
- An extinction-corrected diagnostic diagram based on [O II]/Hβ and [O III]/Hβ ratios, which confirms the small fraction (~23%) of Seyferts and LINERs for ISOCAM 15 μm sources found in other studies (Flores et al. 1999; Fadda et al. 2002; Elbaz et al. 2002).
- A determination of O/H metallicity, which ranges from 8.36 to 8.93 in 12 + log(O/H) for the $z > 0.4$ sample; no obvious trend is found between the IR luminosity and the metallicity.

This study shows that distant LIRGs form a peculiar sequence in the M_B-O/H diagram, which is a broad L–Z relation at bright B absolute luminosities. When compared to local bright disks, at constant metallicity (12 + log(O/H) = 8.67, median value), LIRGs are from 2.5 to 5 mag more luminous, and at constant M_B ($M_B = -21.24$, median value), they are more than two times deficient in metal. These properties can be reproduced with infall models though one has to limit the infall time to avoid overproduction of metals in late time. Models predict a total mass ranging from 10^{11} $M_\odot$ to $\leq 10^{12}$ $M_\odot$, which can be twice of the stellar masses of distant LIRGs derived by Zheng et al. (2004) on the basis of the K band luminosities. In a forthcoming paper (Hammer et al. 2004) we investigate whether LIRG properties could be related to a recent and significant star formation in massive galaxies, including spirals.

Acknowledgements. We are very grateful to Dr. Jarle Brinchmann for the very detailed and valuable comments which have greatly helped us in improving this paper. We thank Dr. Nicolas Gruel for providing us an up-dated version of his software; we are grateful to Dr. Xianzhong Zheng for his comments and suggestions. We thank Dr. David Koch for his help to improve the English language in the text. We also thank Dr. Xiang-Ping Wu for valuable discussions about the cosmological parameters. This work has been supported by grants of the French Ministry of Education and of the K. C. WONG Education Foundation and CNRS.

References

Allende Prieto, C., Lambert, D. L., & Asplund, M. 2001, ApJ, 556, L63
Anders, E., & Grevesse, N. 1989, GeCoA, 53, 197
Aussel, H., Cesarsky, C. J., Elbaz, D., & Starck, J. L. 1999, A&A, 342, 313
Baldwin, J. A., Phillips, M. M., & Terlevich, R. 1981, PASP, 93, 5
Brinchmann, J., Charlot, S., White, S. D. M., et al. 2003, MNRAS, in press [arXiv:astro-ph/0311060]
Cardiel, N., Elbaz, D., Schiavon, R. P., et al. 2003, ApJ, 584, 76
Cesarsky, C. J., Abergel, A., Agnese, P., et al. 1996, A&A, 315, L32
Contini, T., Treyer, M. A., Sullivan, M., & Ellis, R. S. 2002, MNRAS, 330, 75
Coziol, R., Doyon, R., & Demers, S. 2001, MNRAS, 325, 1081
Edmunds, M. G., & Pagel, B. E. J. 1984, MNRAS, 211, 507
Elbaz, D., & Cesarsky, C. J. 2003, Science, 300, 270
Elbaz, D., Cesarsky, C. J., Fadda, D., et al. 1999, A&A, 351, L37
Elbaz, D., Cesarsky, C. J., Chanial, P., et al. 2002, A&A, 384, 848
Elbaz, D., et al. 2004, in preparation
Fadda, D., Flores, H., Hasinger, G., et al. 2002, A&A, 383, 838
Fioc, M., & Rocca-Volmerange, B. 1999 [arXiv:astro-ph/9912179]
Fitzpatrick, E. L. 1999, PASP, 111, 63
Flores, H., Hammer, F., Thuan, T. X., et al. 1999, ApJ, 517, 148
Flores, H., Hammer, F., Elbaz, D., et al. 2004a, A&A, 415, 885
Flores, H., et al. 2004b, in preparation
Franceschini, A., Aussel, H., Cesarsky, C., et al. 2001, A&A, 378, 1
Franceschini, A., Berta, S., Rigopoulou, D., et al. 2003, A&A, 403, 501
Garnett, D. R. 2002, ApJ, 581, 1019
Genzel, R., & Cesarsky, C. J. 2000, ARA&A, 38, 761
Giedke, K., Wilms, J., Lamer, G., et al. 2003, AN, 324, 136
Giedke, K., Wilms, J., Staubert, R., et al. 2001, AGM, 18, 187
Grevesse, N., & Sauval, A. J. 1998, Space Sci. Rev., 85, 161
Gruel, N. 2002, Ph.D. Thesis (http://girafdb.obspm.fr/~lirgsiso)
Hammer, F., Flores, H., Liang, Y. C., et al. 2004, Nature, submitted
Hammer, F., Le Fèvre, O., Lilly, S. J., et al. 1997, ApJ, 481, 49
Hammer, F., Gruel, N., Thuan, T. X., et al. 2001, ApJ, 550, 570
Hopkins, A. M., Miller, C. J., Nichol, R. C., et al. 2003, ApJ, 599, 971
Jacoby, G. H., Hunter, D. A., & Christian, C. A. 1984, ApJS, 56, 257
Jansen, R. A., Franx, M., Fabricant, D., & Caldwell, N. 2000a, ApJS, 126, 271
Jansen, R. A., Fabricant, D., Franx, M., & Caldwell, N. 2000b, ApJS, 126, 331 (J20)
Kauffmann, G., Heckman, T. M., Tremonti, C., et al. 2003, MNRAS, 346, 1055
Kennicutt, R. C., Jr. 1992a, ApJS, 79, 255
Kennicutt, R. C., Jr. 1992b, ApJ, 388, 310 (K92)
Kennicutt, R. C., Jr. 1998, ARA&A, 36, 189
Kewley, L. J., & Dopita, M. A. 2002, ApJS, 142, 35
Kewley, L. J., Heisler, C. A., Dopita, M. A., et al. 2001, ApJS, 132, 37
Kim, D. C., Sanders, D. B., Veilleux, S., et al. 1995, ApJS, 98, 129
Kobulnicky, H. A., & Phillips, A. 2003, ApJ, 599, 1031
Kobulnicky, H. A., Kennicutt, R. C., Jr., & Pizagno, J. L. 1999, ApJ, 514, 544
Kobulnicky, H. A., & Zaritsky, D. 1999, ApJ, 511, 118
Kobulnicky, H. A., Willmer, C. N. A., Weiner, B. J., et al. 2003, ApJ, 599, 1006
Lagache, G., & Dole, H. 2001, A&A, 372, 702
Lamer, G., Wagner, S., Zamorani, G., et al. 2003, AN, 324, 16
Lamareille, F., Mouhcine, M., Contini, T., et al. 2004, MNRAS, in press [arXiv:astro-ph/0401615]
Liang, Y. C., Hammer, F., Flores, H., et al. 2004, A&A, 417, 905
Lilly, S. J., Carollo, C. M., & Stockton, A. N. 2003, ApJ, 597, 730
Lilly, S. J., Le Fèvre, O., Hammer, F., & Crampton, D. 1996, ApJ, 460, L1
Lilly, S. J., Schade, D., Le Fèvre, O., et al. 1998, ApJ, 500, 75
Madau, P., Ferguson, H. C., Dickinson, M. E., et al. 1996, MNRAS, 283, 1388
Maier, C., Meisenheimer, K., & Hippelein, H. 2004, A&A, 418, 475
Marcillac, D., Elbaz, D., et al. 2004, A&A, in preparation
McCall, M. L., Rybski, P. M., & Shields, G. A. 1985, ApJS, 57, 1
McGaugh, S. S. 1991, ApJ, 380, 140

Melbourne, J., & Salzer, J. J. 2002, AJ, 123, 2302
Osterbrock, D. E. 1989, Astrophysics of Gaseous Nebulae and Active Galactic Nuclei (Mill Valley, California: University Science Books)
Poggianti, B. M., Smail, I., Dressler, A., et al. 1999, ApJ, 518, 576
Puget, J.-L., Abergel, A., Bernard, J.-P., et al. 1996, A&A, 308, L5
Puget, J. L., Lagache, G., Clements, D. L., et al. 1999, A&A, 345, 29
Richer, M. G., & McCall, M. L. 1995, ApJ, 445, 642
Salpeter, E. E. 1955, ApJ, 121, 161
Silk, J. 1997, ApJ, 481, 703
Soifer, B. T., Houck, J. R., & Neugebauer, G. 1987, ARA&A, 25, 187
Soifer, B. T., & Mirabel, I. F. 1996, ARA&A, 34, 749
Telles, E., & Erlevich, R. 1997, MNRAS, 286, 183
Vacca, W. D., & Conti, P. S. 1992, ApJ, 401, 543
Veilleux, S., Kim, D. C., Sanders, D. B., et al. 1995, ApJS, 98, 171 (V95)
Veilleux, S., & Osterbrock, D. E. 1987, ApJS, 63, 295
Woosley, S. E., & Weaver, T. A. 1995, ApJS, 101, 181
Zaritsky, D., Kennicutt, R. C., & Huchra, J. P. 1994, ApJ, 420, 87
Zheng, X. Z., Hammer, F., Flores, H., et al. 2004, A&A, 421, 847

Online Material

Table 1. Basic data of the sample galaxies in CFRS 3^h field.

Object	RA	Dec	z	$I_{\rm AB\,phot}$	$I_{\rm AB\,spec}$	Aper	$M_{B,\rm AB}$	Type	f(S15)	$\log(\frac{L_{\rm IR}}{L_\odot})$	$SFR_{\rm IR}$
Slit	(J2000)	(J2000)							μJy		$M_\odot\,{\rm yr}^{-1}$
(1)	(2)	(3)	(4)	(5)	(6)	(7)	(8)	(9)	(10)	(11)	(12)
03.1153 CFRS01	3 02 52.12	+00 12 56.3	0.0000	21.64	21.89	1.26	–	Star	0.0	0.00	0.00
03.1309 CFRS02	3 02 52.01	+00 10 33.0	0.6172	20.62	21.13	1.60	−21.49	EL	507.0	11.86 ± 0.08	124.86
03.1324 CFRS03	3 02 50.72	+00 10 41.0	0.1748	21.80	21.20	0.58	−17.19	EL	0.0	0.00	0.00
03.1183 CFRS04	3 02 49.37	+00 13 7.5	0.3870	21.90	21.93	1.03	−18.37	Ear	419.0	11.26 ± 0.10	31.06
03.1188 CFRS05	3 02 48.85	+00 12 30.2	9999	21.68	23.58	5.75	–	?	0.0	–	–
03.1349 CFRS06	3 02 49.08	+00 10 1.8	0.6169	20.87	21.47	1.74	−21.16	EL	334.0	11.56 ± 0.11	62.07
03.1522 CFRS07	3 02 47.31	+00 13 7.2	0.5870	22.02	23.18	2.91	−19.59	?	213.0	11.21 ± 0.12	28.06
03.0422 CFRS08	3 02 46.29	+00 13 53.6	0.7154	21.21	21.97	2.01	−21.22	EL	331.0	11.72 ± 0.11	90.80
03.0641 CFRS09	3 02 45.93	+00 11 25.7	0.2613	20.03	20.81	2.05	−19.11	EL	0.0	0.00	0.00
03.0445 CFRS10	3 02 44.57	+00 12 20.1	0.5276	20.64	21.20	1.70	−21.23	EL	220.0	11.17 ± 0.19	25.67
03.1541 CFRS11	3 02 43.38	+00 12 9.5	0.6895	21.85	21.80	1.06	−20.52	EL	425.0	11.86 ± 0.10	123.54
03.0495 CFRS12	3 02 41.54	+00 14 42.9	0.2614	19.43	20.01	2.05	−19.82	EL	323.0	10.60 ± 0.12	6.81
03.0711 CFRS13	3 02 42.31	+00 10 1.4	0.2615	21.04	21.52	1.55	−18.54	EL	180.0	10.32 ± 0.22	3.56
03.0507 CFRS14	3 02 40.44	+00 14 3.8	0.4652	20.95	21.33	1.42	−20.47	EL	195.0	11.04 ± 0.30	19.00
03.1531 CFRS15	3 02 39.72	+00 13 21.2	0.7163	21.81	23.56	4.96	−20.52	EL	293.0	11.65 ± 0.11	76.85
03.0533 CFRS16	3 02 38.80	+00 14 17.5	0.8274	21.47	21.98	1.60	−21.38	EL	401.0	12.10 ± 0.10	215.84
03.0776 CFRS17	3 02 39.18	+00 10 35.1	0.8837	22.37	22.88	1.60	−20.69	EL	177.0	11.59 ± 0.20	67.38
03.0799 CFRS18	3 02 38.21	+00 11 50.1	9999	24.04	25.47	3.73	–	?	0.0	–	–
03.0828 CFRS19	3 02 37.44	+00 11 17.4	0.3310	22.44	23.29	2.19	−17.83	EL	305.0	10.88 ± 0.12	12.95
03.0569 CFRS20	3 02 35.63	+00 14 12.0	0.1810	21.33	22.32	2.49	−16.73	?	176.0	9.88 ± 0.23	1.32
03.0578 CFRS21	3 02 35.19	+00 14 10.1	0.2189	20.79	22.27	3.91	−18.62	EL	167.0	10.07 ± 0.23	2.04
03.0589 CFRS22	3 02 34.41	+00 13 31.9	0.7172	22.18	22.53	1.38	−20.25	EL	0.0	0.00	0.00
03.5004 CFRS23	3 02 34.82	+00 12 42.9	0.0875	17.74	19.63	5.68	–	EL	2089.0	10.29 ± 0.08	3.35
03.0916 CFRS24	3 02 33.71	+00 11 37.7	1.0300	21.31	22.05	1.98	–	QSO	219.0	12.04 ± 0.12	–
03.0932 CFRS25	3 02 33.14	+00 11 5.2	0.6478	21.37	22.21	2.17	−20.73	EL	529.0	11.94 ± 0.09	150.83
03.0006 CFRS26	3 02 31.53	+00 14 3.3	0.8836	23.29	23.94	1.82	−19.77	EL	183.0	11.61 ± 0.23	69.65
03.0015 CFRS27	3 02 30.73	+00 12 58.6	0.1980	21.68	21.64	0.96	−16.60	Ear	0.0	0.00	0.00
03.0138 CFRS28	3 02 30.82	+00 11 1.8	0.4797	20.09	20.46	1.41	−20.87	Ear	0.0	0.00	0.00
03.0035 CFRS29	3 02 29.41	+00 12 59.8	0.8804	21.16	21.99	2.15	−21.88	EL	318.0	12.03 ± 0.12	182.36
03.0149 CFRS30	3 02 29.51	+00 9 17.2	0.2510	20.74	22.29	4.17	−18.92	EL	0.0	0.00	0.00
03.0062 CFRS31	3 02 27.20	+00 13 56.6	0.8272	20.96	21.79	2.15	−21.85	EL	228.0	11.67 ± 0.15	80.51
03.0174 CFRS32	3 02 27.53	+00 10 57.2	0.5251	22.31	23.06	2.00	−19.11	EL	212.0	11.16 ± 0.26	24.66
03.0186 CFRS33	3 02 26.86	+00 10 55.1	0.5254	22.01	22.88	2.23	−19.32	EL	185.0	11.08 ± 0.25	20.58
03.0085 CFRS34	3 02 25.24	+00 13 24.8	0.6089	22.00	22.29	1.31	−19.96	EL	203.0	11.21 ± 0.20	27.66

Note: The magnitude of CFRS23 is $R_{\rm AB}$ and is not $I_{\rm AB}$.

Table 2. Basic data of the sample galaxies in UDSR and UDSF fields.

Object	RA	Dec	z	$R_{\rm AB\,phot}$	$R_{\rm AB\,spec}$	Aper	$M_{B,\rm AB}$	Type	f(S15)	$\log(\frac{L_{\rm IR}}{L_\odot})$	$SFR_{\rm IR}$
Slit	(J2000)	(J2000)							μJy		$M_\odot\,{\rm yr}^{-1}$
(1)	(2)	(3)	(4)	(5)	(6)	(7)	(8)	(9)	(10)	(11)	(12)
UDSR01	3 15 02.4	−55 21 25	0.1025	20.94	21.72	2.05	−17.03	EL	91.2	8.91 ± 0.20	0.14
UDSR02	3 14 54.6	−55 22 17	0.9334	23.16	23.72	1.67	−20.72	EL	0.0	0.00	0.00
UDSR03	3 14 51.6	−55 22 27	9999	23.28	23.77	1.57	–	?	0.0	–	–
UDSR04	3 14 55.9	−55 21 34	0.4501	22.97	23.21	1.25	−19.42	EL	231.5	10.96 ± 0.18	15.68
UDSR05	3 15 07.1	−55 19 45	1.0657	23.22	23.74	1.61	−22.18	EL	249.6	12.03 ± 0.24	183.10
UDSR06	3 15 05.1	−55 19 51	0.1836	19.88	20.32	1.50	−19.30	EL	345.5	10.08 ± 0.12	2.07
UDSR07	3 14 57.3	−55 20 31	0.5507	23.91	24.36	1.51	−19.27	?	251.9	11.10 ± 0.19	21.85
UDSR08	3 14 55.2	−55 20 31	0.7291	21.60	22.18	1.71	−21.52	EL	235.7	11.32 ± 0.21	35.66
UDSR09	3 14 56.1	−55 20 08	0.3884	19.53	19.95	1.47	−21.75	EL	608.9	11.30 ± 0.08	34.21
UDSR10	3 14 43.9	−55 21 35	0.6798	20.84	21.48	1.80	−22.29	EL	495.2	11.75 ± 0.13	96.92
UDSR11	3 14 45.7	−55 20 53	0.1660	19.81	20.38	1.69	−19.20	EL	252.1	9.82 ± 0.13	1.15
UDSR12	3 14 37.5	−55 21 44	0.1654	20.76	21.15	1.43	−18.23	EL	226.7	9.77 ± 0.15	1.01
UDSR13	3 14 35.9	−55 21 35	0.1666	20.78	21.12	1.37	−18.15	EL	53.0	9.14 ± 0.23	0.24
UDSR14	3 14 43.3	−55 20 11	0.8150	21.56	22.29	1.96	−22.22	EL	200.1	11.34 ± 0.24	38.00
UDSR15	3 14 36.3	−55 21 02	0.4949	21.51	22.19	1.87	−20.61	EL	235.6	11.03 ± 0.19	18.40
UDSR16	3 14 33.1	−55 21 01	0.1662	20.86	21.15	1.31	−18.29	EL	180.4	9.67 ± 0.16	0.82
UDSR17	3 14 41.3	−55 19 24	0.9680	22.51	23.05	1.64	−22.25	EL	386.2	12.10 ± 0.19	219.01
UDSR18a	3 14 53.5	−55 17 26	9999	23.33	23.24	0.92	–	?	0.0	–	–
UDSR18b	3 14 53.4	−55 17 24	9999	24.43	23.74	0.53	–	?	247.1	–	–
UDSR19a	3 14 39.5	−55 19 03	0.0000	22.53	22.48	0.95	–	Star	174.7	0.00	0.00
UDSR19b	3 14 39.3	−55 19 01	0.0000	22.66	22.98	1.34	–	Star	174.7	0.00	0.00
UDSR20	3 14 41.1	−55 18 40	0.7660	21.79	23.12	3.40	−21.87	EL	214.4	11.32 ± 0.23	35.81
UDSR21	3 14 43.6	−55 17 50	0.4655	22.54	23.17	1.79	−19.52	EL	56.8	10.24 ± 0.26	3.01
UDSR22	3 14 48.2	−55 16 57	0.4970	21.92	23.15	3.10	–	?	0.0	0.00	0.00
UDSR23	3 14 32.1	−55 19 02	0.7094	21.12	21.45	1.36	−21.70	EL	271.1	11.38 ± 0.20	40.96
UDSR24	3 14 33.7	−55 18 40	0.3136	–	20.46	–	–	Ear	164.0	10.36 ± 0.18	3.96
UDSR25a	3 14 24.8	−55 19 35	0.5816	20.48	20.61	1.13	−22.08	EL	702.5	11.85 ± 0.09	122.08
UDSR25b	3 14 24.8	−55 19 36	9999	21.11	–	–	–	?	0.0	–	–
UDSR26	3 14 36.7	−55 17 32	0.3841	21.08	21.68	1.74	−20.27	EL	82.5	10.27 ± 0.23	3.17
UDSR27	3 14 29.6	−55 18 22	0.6429	22.19	22.18	0.99	−20.61	EL	128.9	10.80 ± 0.23	10.93
UDSR28	3 14 20.7	−55 19 20	0.5210	20.65	21.01	1.39	−21.76	Ear	231.5	11.04 ± 0.18	18.65
UDSR29	3 14 27.4	−55 18 06	9999	23.52	23.43	0.92	–	?	0.0	–	–
UDSR30	3 14 26.7	−55 17 51	0.9590	22.69	23.08	1.43	−21.45	EL	408.7	12.12 ± 0.18	225.95
UDSR31	3 14 25.6	−55 17 51	0.9530	22.84	23.17	1.36	−21.81	?	274.5	11.80 ± 0.21	109.40
UDSR32	3 14 30.3	−55 16 53	0.5841	22.33	22.96	1.79	−19.98	EL	137.3	10.77 ± 0.23	10.13
UDSF01	3 13 27.6	−55 05 53	0.4656	20.41	21.22	2.11	−21.61	EL	86.6	10.45 ± 0.11	4.82
UDSF02	3 13 23.3	−55 05 15	0.7781	22.57	24.00	3.73	−21.43	EL	47.0	10.43 ± 0.12	4.59
UDSF03	3 13 33.6	−55 04 27	0.5532	21.54	22.65	2.78	−20.86	EL	0.0	<10.81	<11.14
UDSF04	3 13 28.5	−55 04 45	0.9620	22.99	23.44	1.51	−21.54	EL	246.8	11.75 ± 0.12	97.17
UDSF05	3 13 30.4	−55 04 17	0.1658	19.85	20.46	1.75	−19.12	Ear	0.0	<9.59	<0.69
UDSF06	3 13 30.2	−55 04 04	0.6928	21.91	22.31	1.45	−21.52	EL	150.0	10.97 ± 0.33	15.97
UDSF07	3 13 17.3	−55 05 16	0.7014	22.37	22.95	1.71	−20.70	EL	154.3	10.99 ± 0.12	16.77
UDSF08	3 13 14.2	−55 05 37	0.7075	22.30	22.96	1.84	−21.03	EL	137.7	10.91 ± 0.12	14.01
UDSF09	3 13 18.0	−55 04 57	0.2273	19.99	20.93	2.38	−19.71	Ear	68.9	9.58 ± 0.10	0.69
UDSF10	3 13 12.6	−55 05 11	9999	24.04	24.31	1.28	–	?	0.0	–	–
UDSF11	3 13 23.3	−55 03 33	0.0937	19.36	19.93	1.69	−18.39	EL	155.4	9.06 ± 0.09	0.23
UDSF12	3 13 07.7	−55 05 26	0.7388	22.45	23.13	1.87	−21.39	EL	331.1	11.56 ± 0.13	62.83
UDSF13	3 13 14.2	−55 04 21	0.7605	23.54	24.37	2.15	−20.44	EL	906.6	12.38 ± 0.11	408.45
UDSF14	3 13 09.7	−55 04 33	0.8190	23.08	23.92	2.17	−21.08	EL	64.1	10.65 ± 0.13	7.70
UDSF15	3 13 10.7	−55 04 06	0.2302	22.60	23.55	2.40	−17.57	EL	0.0	<9.95	<1.49
UDSF16	3 13 08.0	−55 04 18	0.4548	20.39	21.11	1.94	−21.47	EL	137.6	10.68 ± 0.11	8.16
UDSF17	3 13 08.6	−55 03 57	0.8100	21.45	22.16	1.92	−22.42	EL	256.9	11.52 ± 0.14	56.97
UDSF18	3 13 16.5	−55 02 27	0.4620	21.42	22.08	1.84	−20.60	EL	170.0	10.81 ± 0.10	11.03
UDSF19	3 13 09.8	−55 03 08	0.5476	20.68	21.20	1.61	−21.94	EL	611.3	11.67 ± 0.11	80.86
UDSF20	3 13 19.0	−55 01 42	0.8424	22.30	23.25	2.40	–	EL	117.2	11.04 ± 0.14	18.84
UDSF21	3 13 04.5	−55 03 12	0.6980	21.78	22.41	1.79	−21.35	EL	0.0	<10.97	<16.20
UDSF22	3 12 51.7	−55 04 39	0.2298	20.48	20.88	1.45	−19.38	EL	134.1	9.89 ± 0.09	1.38
UDSF23	3 13 05.0	−55 02 36	1.0404	22.76	23.26	1.58	−21.83	?	0.0	<11.58	<65.47
UDSF24	3 13 04.8	−55 02 24	1.1586	21.92	23.13	3.05	−23.31	EL	159.7	11.91 ± 0.16	138.87
UDSF25	3 13 07.3	−55 01 56	0.8094	23.32	24.94	4.45	−20.42	EL	94.2	10.86 ± 0.13	12.52
UDSF26a	3 12 58.0	−55 02 53	0.7027	23.07	24.63	4.21	−21.60	EL	0.0	<10.98	<16.31
UDSF26b	3 12 57.5	−55 02 48	0.7023	21.16	21.83	1.85	−20.62	EL	163.3	11.03 ± 0.13	18.38
UDSF27a	3 12 58.4	−55 02 34	9999	23.43	23.98	1.66	–	?	108.1	–	–
UDSF27b	3 12 58.2	−55 02 32	9999	23.72	24.33	1.75	–	?	0.0	–	–
UDSF28	3 12 51.8	−55 02 57	0.6612	21.31	22.25	2.38	−21.84	EL	321.4	11.40 ± 0.12	42.96
UDSF29a	3 12 50.5	−55 03 1	9999	24.18	–	–	–	?	0.0	–	–
UDSF29b	3 12 50.2	−55 02 59	0.6619	22.64	23.37	1.96	−20.45	EL	353.9	11.47 ± 0.12	51.34
UDSF30	3 12 44.9	−55 03 27	9999	23.31	22.79	0.62	–	?	114.6	–	–
UDSF31	3 12 44.0	−55 03 21	0.6868	22.39	22.93	1.64	−20.57	EL	192.8	11.10 ± 0.13	21.71
UDSF32	3 12 53.3	−55 01 43	0.7268	23.16	23.78	1.77	−19.73	EL	226.3	11.27 ± 0.13	32.28
UDSF33	3 12 53.9	−55 01 28	9999	21.07	22.17	2.75	–	?	295.7	–	–

Table 3. Redshift-identification and spectral types of the galaxies in the three fields. "ELGs" means "Emission Line Galaxies", "ETGs" means "Early-Type Galaxies", "z-poor" means the redshift can be gotten even the Type is not clear from the spectrum.

Fields	Objects	ELGs			ETGs	Stars	QSO	z-	z-	Redshifts		Redshift	median
		ISO		non-ISO				poor	unknown	ISO	non-ISO	identified	z
		$z > 0.4$	$z \leq 0.4$										
CFRS	34	16	5	4	3	1	1	2	2	25	7	94.12 %	0.525
UDSR	35	14	8	1	2	2	0	3	5	28	2	85.71 %	0.521
UDSF	36	21	2	4	2	0	0	1	6	24	6	83.33 %	0.698
Three fields	105	51	15	9	7	3	1	6	13	77	15	87.62 %	0.587

Table 4. Measured emission line fluxes (F_λ) in unit of 10^{-17} (ergs cm^{-2} s^{-1}) and the errors in percent for the high-z EL galaxies. "9997" means the line is blended with strong sky line, "9998" means there is no corresponding emission line detected at the line position, and "9999" means the line is shifted outside of the rest-frame wavelength range. "o5" means [O III]$_{5007}$, and "o4" means [O III]$_{4959}$.

Slit	z	[O II]$_{3727}$	$e_{[\mathrm{O\,II}]}$%	Hγ	$e_{\mathrm{H}\gamma}$%	Hβ	$e_{\mathrm{H}\beta}$%	[O III]$_{5007}$	e_{o5}%	[O III]$_{4959}$	e_{o4}%
(1)	(2)	(3)	(4)	(5)	(6)	(7)	(8)	(9)	(10)	(11)	(12)
CFRS											
2	0.6172	14.66	0.02	1.99	0.12	6.30	0.10	9.49	0.06	9998	9998
6	0.6169	6.55	0.02	1.63	0.10	5.04	0.10	8.49	0.06	2.28	0.17
8	0.7154	4.28	0.04	1.38	0.13	4.37	0.10	9999	9999	9999	9999
10	0.5276	7.57	0.05	1.68	0.08	4.29	0.07	0.90	0.16	9998	9998
11	0.6895	5.10	0.09	1.05	0.20	3.92	0.08	1.18	0.25	9998	9998
12	0.2614	9999	9999	3.78	0.13	10.09	0.05	30.90	0.02	10.97	0.04
14	0.4652	16.81	0.02	2.09	0.11	6.87	0.05	6.55	0.10	2.55	0.17
15	0.7163	2.86	0.08	2.06	0.16	9997	9997	9998	9998	9998	9998
16	0.8274	11.42	0.04	1.64	0.15	9999	9999	9999	9999	9999	9999
17	0.8837	7.14	0.04	0.58	0.19	2.05	0.11	0.58	0.40	9998	9998
19	0.3310	9999	9999	0.29	0.16	0.77	0.08	1.44	0.10	0.43	0.32
22	0.7172	4.99	0.05	0.63	0.28	9997	9997	9999	9999	9999	9999
25	0.6478	6.34	0.04	1.14	0.17	2.87	0.15	2.85	0.11	9998	9998
26	0.8836	2.05	0.15	9998	9998	9999	9999	9999	9999	9999	9999
29	0.8804	2.38	0.16	9998	9998	9999	9999	9999	9999	9999	9999
31	0.8272	5.61	0.05	1.46	0.15	9999	9999	9999	9999	9999	9999
32	0.5251	1.13	0.13	9998	9998	0.31	0.10	0.32	0.16	9999	9999
33	0.5254	2.80	0.04	0.31	0.50	0.98	0.10	0.56	0.16	9998	9998
34	0.6089	9.97	0.04	0.76	0.15	9997	9997	2.12	0.22	9998	9998
UDSR											
2	0.9334	5.39	0.05	1.01	0.30	9999	9999	9999	9999	9999	9999
4	0.4501	3.71	0.08	9998	9998	0.58	0.15	1.65	0.13	0.51	0.23
5	1.0657	5.92	0.06	9999	9999	9999	9999	9999	9999	9999	9999
8	0.7291	23.27	0.02	4.07	0.07	9.52	0.06	10.88	0.05	5.03	0.07
9	0.3884	5.83	0.08	9998	9998	0.47	0.10	9.34	0.05	3.10	0.15
10	0.6798	11.13	0.06	2.47	0.15	7.02	0.09	5.24	0.13	1.83	0.15
14	0.8150	18.13	0.04	3.32	0.18	9.29	0.50	8.93	0.10	3.01	0.15
15	0.4949	9999	9999	1.20	0.10	4.02	0.15	3.92	0.06	1.32	0.12
17	0.9680	2.28	0.25	9998	9998	9999	9999	9999	9999	9999	9999
20	0.7660	16.57	0.02	2.33	0.09	6.48	0.06	9.81	0.08	9998	9998
21	0.4655	2.03	0.13	9998	9998	0.45	0.40	4.75	0.10	9998	9998
23	0.7094	13.35	0.02	2.22	0.11	7.01	0.07	4.63	0.10	1.57	0.15
26	0.3841	3.61	0.10	9998	9998	1.25	0.20	1.04	0.16	9998	9998
27	0.6429	4.13	0.08	9998	9998	9997	9997	9998	9998	9998	9998
30	0.9590	2.85	0.18	9998	9998	9999	9999	9999	9999	9999	9999
32	0.5841	8.45	0.05	0.89	0.25	2.64	0.10	4.47	0.09	9998	9998
UDSF											
1	0.4656	30.79	0.02	3.74	0.08	9.42	0.04	13.98	0.11	5.11	0.12
2	0.7781	1.82	0.07	9999	9999	0.54	0.40	0.36	0.40	9998	9998
3	0.5532	2.66	0.09	9999	9999	1.90	0.13	1.45	0.30	9998	9998
4	0.9620	2.985	0.09	9998	9998	9999	9999	9999	9999	9999	9999
6	0.6928	4.70	0.11	9998	9998	9998	9998	9999	9999	9998	9998
7	0.7014	3.79	0.08	0.88	0.23	2.42	0.16	1.19	0.30	9998	9998
8	0.7075	2.15	0.08	9998	9998	9998	9998	9998	9998	9998	9998
12	0.7388	4.44	0.06	9998	9998	1.84	0.11	9998	9998	9998	9998
13	0.7605	5.62	0.08	0.51	0.30	1.58	0.40	21.55	0.05	6.02	0.10
14	0.8190	1.39	0.50	9998	9998	9998	9998	9998	9998	9998	9998
15	0.2302	9999	9999	0.74	0.10	1.87	0.10	3.92	0.05	1.49	0.11
16	0.4548	3.79	0.07	1.15	0.24	3.88	0.09	2.35	0.30	9998	9998
17	0.8100	10.57	0.06	1.45	0.33	4.09	0.18	1.56	0.17	9998	9998
18	0.4620	12.93	0.03	2.09	0.14	5.36	0.05	2.93	0.18	0.95	0.30
19	0.5476	8.21	0.05	3.61	0.10	11.09	0.07	7.72	0.40	9998	9998
20	0.8424	2.72	0.50	9998	9998	9999	9999	9999	9999	9999	9999
21	0.6980	11.56	0.03	2.27	0.22	5.66	0.10	6.20	0.13	9998	9998
24	1.1586	13.61	0.04	9999	9999	9999	9999	9999	9999	9999	9999
25	0.8094	6.00	0.04	9998	9998	9999	9999	9999	9999	9999	9999
26a	0.7027	3.76	0.01	1.24	0.30	2.95	0.05	22.65	0.01	5.89	0.05
26b	0.7023	35.75	0.01	5.32	0.06	12.85	0.05	25.34	0.01	9.03	0.05
28	0.6612	5.49	0.05	0.61	0.25	1.89	0.20	15.85	0.04	5.00	0.09
29	0.6619	2.44	0.09	0.36	0.40	1.21	0.20	1.02	0.26	9998	9998
31	0.6868	2.52	0.11	9999	9999	2.13	0.30	1.73	0.10	9998	9998
32	0.7268	2.25	0.10	9998	9998	0.65	0.20	0.51	0.20	9998	9998

Table 5. Measured emission line fluxes (F_λ) in unit of 10^{-17} (ergs cm^{-2} s^{-1}) and the errors in percent in the low-z EL galaxies in CFRS/UDSR/UDSF fields (C/R/F).

Slit	Hβ	$e_{\rm H\beta}$%	[O III]$_5$	e_{o5}%	[O III]$_4$	e_{o4}%	Hα	$e_{\rm H\alpha}$%	[N II]$_2$	e_{n2}%	[N II]$_1$	e_{n1}%	[S II]$_1$	e_{s1}%	[S II]$_2$	e_{s2}%
(1)	(2)	(3)	(4)	(5)	(6)	(7)	(8)	(9)	(10)	(11)	(12)	(13)	(14)	(15)	(16)	(17)
C																
3	9999	9999	1.31	0.19	9998	9998	3.45	0.17	0.54	0.21	9998	9998	9997	9997	9997	9997
9	2.21	0.11	0.92	0.18	0.31	0.06	10.25	0.09	3.53	0.12	1.18	0.12	<1.38	–	<1.65	–
12	10.09	0.05	30.90	0.02	10.97	0.04	9999	9999	9999	9999	9999	9999	9999	9999	9999	9999
13	4.49	0.04	1.95	0.10	0.65	0.11	13.58	0.04	5.78	0.12	1.04	0.12	3.56	0.10	1.96	0.19
19	0.77	0.08	1.44	0.10	0.43	0.32	3.41	0.14	1.37	0.27	9998	9998	9997	9997	9997	9997
21	1.23	0.16	1.77	0.15	0.61	0.15	8.76	0.05	1.80	0.36	1.06	0.32	1.80	0.17	2.07	0.14
23	9999	9999	9999	9999	9999	9999	25.77	0.01	37.30	0.01	11.31	0.03	5.68	0.08	5.40	0.12
30	4.76	0.06	5.43	0.04	1.87	0.04	17.18	0.04	3.49	0.12	1.35	0.13	3.95	0.18	2.61	0.15
R																
1	4.83	0.10	13.68	0.02	4.60	0.05	17.06	0.02	2.21	0.10	9998	9998	2.95	0.50	2.68	0.10
6	4.62	0.14	4.31	0.09	9998	9998	19.35	0.03	12.14	0.08	3.49	0.10	6.83	0.15	4.22	0.40
11	4.42	0.05	3.22	0.08	0.94	0.06	13.92	0.03	8.21	0.03	9998	9998	6.16	0.08	7.19	0.11
12	9999	9999	9999	9999	9999	9999	11.23	0.03	6.16	0.07	9998	9998	4.42	0.12	2.73	0.18
13	9999	9999	9999	9999	9999	9999	4.29	0.08	2.57	0.10	9998	9998	1.49	0.30	0.70	0.30
16	9999	9999	9999	9999	9999	9999	24.90	0.01	5.55	0.04	9998	9998	7.62	0.04	4.81	0.10
F																
11	10.43	0.03	6.11	0.07	9998	9998	30.10	0.01	13.76	0.02	7.50	0.06	10.32	0.07	8.59	0.06
15	1.87	0.10	3.92	0.05	1.49	0.11	7.98	0.04	0.75	0.32	0.60	0.40	1.71	0.16	0.82	0.40
22	9999	9999	4.62	0.08	1.46	0.21	30.40	0.02	9.95	0.05	2.88	0.17	7.69	0.05	6.04	0.13

Notes: [O III]$_5$ and o5 mean [O III] λ5007; [O III]$_4$ and o4 mean [O III] λ4959; [N II]$_2$ and n2 mean [N II] λ6583; [N II]$_1$ and n1 mean [N II] λ6548; [S II]$_1$ and s1 mean [S II] λ6716; [S II]$_2$ and s2 mean [S II] λ6731. The Hγ emission line fluxes of CFRS12, 19 and UDSF15 are given in Table 4.

Table 6. The extinction A_V(Balmer), A_V(IR), the $SFR_{\rm H\alpha}$, "flux blending" factor "FB", the continuum colors, some important emission line ratios, the oxygen abundance in ISM and the spectral types from the diagnostic diagrams ("H" for H II region galaxies, "L" for LINERs and "S" for Seyfert 2) for the sample galaxies. [O II] = [O II] λ3727, [O III] = [O III] λ4959 + [O III] λ5007, and [O III]$_5$ = [O III] λ5007. "FB" (Col. 4) refers to the possible flux blending: "3" means "possible flux blending", "1" means "isolated", "0" means "non-ISO detected". For oxygen abundances (Col. 12), the right up-description "L" means the values are determined from R_3 parameter. The uncertainties of the line ratios and metallicity are from the uncertainties of extinction and emission line flux measurements. The typical 30% uncertainty of $SFR_{\rm IR}$ will result in a typical 0.03 dex discrepancy on the derived values.

Slit	A_V Balmer	$SFR_{\rm H\alpha}$ $M_\odot$ yr^{-1}	FB	A_V IR	$\frac{C4861}{C3660}$	$\log(\frac{[\rm O\,II]}{[\rm O\,III]_5})$	$\log(\frac{[\rm O\,II]}{\rm H\beta})$	$\log(\frac{[\rm O\,III]}{\rm H\beta})$	$\log(R_{23})$	$\log(O_{32})$	12+$\log(\frac{\rm O}{\rm H})$	T
(1)	(2)	(3)	(4)	(5)	(6)	(7)	(8)	(9)	(10)	(11)	(12)	(13)
C												
2	2.52 ± 0.96	$56.08^{+58.51}_{-52.41}$	3	3.24	1.81	0.67 ± 0.10	0.79 ± 0.08	0.24 ± 0.03	0.89 ± 0.07	-0.54 ± 0.10	8.37 ± 0.11	H
6	2.35 ± 0.96	$40.35^{+40.35}_{-42.11}$	3	2.74	1.11	0.29 ± 0.10	0.47 ± 0.09	0.30 ± 0.03	0.69 ± 0.05	-0.17 ± 0.10	8.69 ± 0.06	H
8	2.54 ± 1.17	$71.75^{+90.79}_{-67.17}$	1	2.75	2.17	–	–	–	–	–	–	–
10	1.11 ± 0.93	$6.05^{+6.13}_{-4.24}$	3	2.43	1.48	1.28 ± 0.15	0.56 ± 0.07	-0.60 ± 0.13	0.59 ± 0.07	-1.16 ± 0.15	8.72 ± 0.07	H
11	3.59 ± 1.40	$97.17^{+146.9}_{-95.20}$	3	3.81	1.23	1.20 ± 0.14	0.61 ± 0.08	-0.47 ± 0.11	0.64 ± 0.07	-1.07 ± 0.14	8.67 ± 0.09	H
12	1.41 ± 0.90	$4.54^{+4.44}_{-3.55}$	1	1.78	0.97	–	–	0.58 ± 0.01	–	–	8.34 ± 0.01^L	H
14	2.75 ± 0.90	$35.49^{+34.70}_{-33.71}$	1	2.18	1.32	0.73 ± 0.07	0.67 ± 0.04	0.06 ± 0.04	0.77 ± 0.04	-0.61 ± 0.07	8.55 ± 0.05	H
17	3.24 ± 1.48	$96.17^{+154.1}_{-93.30}$	1	2.91	1.73	1.52 ± 0.20	0.92 ± 0.09	-0.48 ± 0.17	0.93 ± 0.09	-1.39 ± 0.20	8.15 ± 0.20	L
19	1.34 ± 1.34	$0.59^{+0.85}_{-0.45}$	3	3.97	–	–	–	0.32 ± 0.05	–	–	8.57 ± 0.05^L	H
25	$1.04^{+1.47}_{-1.04}$	$7.89^{+12.55}_{-5.35}$	1	3.77	2.09	0.50 ± 0.15	0.48 ± 0.13	0.10 ± 0.05	0.63 ± 0.11	-0.38 ± 0.15	8.73 ± 0.19	H
32	–	–	1	3.97	6.24	1.13 ± 0.13	1.08 ± 0.10	0.07 ± 0.07	1.12 ± 0.09	-1.01 ± 0.13	7.78 ± 0.25	L
33	$2.59^{+3.27}_{-2.59}$	$8.83^{+31.30}_{-8.30}$	1	3.37	2.31	1.19 ± 0.12	0.89 ± 0.09	-0.18 ± 0.07	0.93 ± 0.08	-1.07 ± 0.12	8.22 ± 0.16	L
R												
4	–	–	3	3.97	–	0.94 ± 0.15	1.32 ± 0.13	0.51 ± 0.05	1.38 ± 0.11	-0.81 ± 0.15	7.05 ± 0.41	L
6	1.78 ± 1.53	$1.03^{+1.71}_{-0.88}$	1	2.42	–	–	–	0.05 ± 0.04	–	–	8.83 ± 0.04^L	L?
8	$0.55^{+0.60}_{-0.55}$	$16.05^{+10.39}_{-7.23}$	1	1.30	1.31	0.52 ± 0.06	0.56 ± 0.05	0.16 ± 0.02	0.70 ± 0.04	-0.40 ± 0.06	8.66 ± 0.04	H
9	–	–	1	3.99	2.44	0.39 ± 0.10	1.61 ± 0.09	1.35 ± 0.03	1.80 ± 0.06	-0.26 ± 0.10	–	S
10	1.82 ± 1.13	$42.08^{+51.67}_{-36.25}$	1	2.59	1.10	0.71 ± 0.11	0.53 ± 0.08	-0.05 ± 0.06	0.63 ± 0.06	-0.58 ± 0.11	8.71 ± 0.07	H
14	$1.72^{+3.44}_{-1.72}$	$84.41^{+314.8}_{-71.30}$	1	0.98	1.39	0.45 ± 0.48	0.42 ± 0.42	0.09 ± 0.07	0.58 ± 0.29	-0.33 ± 0.48	8.78 ± 0.26	H
15	2.91 ± 1.19	$37.44^{+48.12}_{-35.84}$	1	2.25	1.20	–	–	0.07 ± 0.05	–	–	8.81 ± 0.05	–
20	1.68 ± 0.70	$84.95^{+64.50}_{-71.16}$	1	0.89	2.23	0.36 ± 0.07	0.52 ± 0.05	0.29 ± 0.04	0.72 ± 0.03	-0.23 ± 0.07	8.65 ± 0.04	H
23	2.49 ± 0.84	$74.07^{+67.79}_{-69.11}$	1	1.94	1.30	0.75 ± 0.08	0.53 ± 0.06	-0.09 ± 0.04	0.62 ± 0.05	-0.62 ± 0.08	8.72 ± 0.05	H
26	–	–	0	2.34	2.33	0.89 ± 0.21	0.76 ± 0.17	0.00 ± 0.07	0.83 ± 0.15	-0.76 ± 0.21	8.44 ± 0.24	H
32	2.13 ± 1.72	$14.98^{+27.94}_{-13.49}$	1	1.76	0.84	0.54 ± 0.10	0.73 ± 0.08	0.32 ± 0.04	0.87 ± 0.06	-0.41 ± 0.10	8.42 ± 0.09	H
F												
1	1.04 ± 0.58	$11.26^{+7.07}_{-7.61}$	3	0.25	1.22	0.38 ± 0.06	0.55 ± 0.03	0.29 ± 0.05	0.74 ± 0.03	-0.26 ± 0.06	8.63 ± 0.03	H
2	–	–	1	1.16	2.71	0.88 ± 0.53	0.68 ± 0.42	-0.08 ± 0.23	0.75 ± 0.36	-0.75 ± 0.53	8.56 ± 0.49	H
3	–	–	1	1.87	2.10	0.54 ± 0.19	0.39 ± 0.12	-0.03 ± 0.14	0.53 ± 0.09	-0.42 ± 0.19	8.82 ± 0.07	H
7	$1.58^{+2.15}_{-1.58}$	$11.43^{+26.58}_{-9.38}$	3	1.93	1.53	0.79 ± 0.20	0.44 ± 0.14	-0.22 ± 0.13	0.53 ± 0.11	-0.66 ± 0.20	8.81 ± 0.10	H
12	–	–	1	3.21	3.45	–	–	–	–	–	–	–
13	$2.39^{+3.24}_{-2.39}$	$27.43^{+96.28}_{-25.37}$	3	2.39	2.80	-0.23 ± 0.39	0.86 ± 0.34	1.21 ± 0.05	1.37 ± 0.15	0.12 ± 0.39	–	S
15	1.06 ± 0.92	$0.51^{+0.50}_{-0.35}$	0	2.06	–	–	–	0.41 ± 0.03	–	–	8.50 ± 0.03^L	H
16	2.93 ± 1.66	$31.65^{+56.95}_{-30.34}$	1	1.68	1.45	0.46 ± 0.17	0.21 ± 0.08	-0.13 ± 0.15	0.37 ± 0.07	-0.33 ± 0.17	8.93 ± 0.04	H
17	$1.78^{+2.27}_{-1.78}$	$38.18^{+93.75}_{-32.63}$	1	2.15	1.52	1.15 ± 0.19	0.69 ± 0.15	-0.33 ± 0.08	0.73 ± 0.14	-1.03 ± 0.19	8.56 ± 0.20	H
18	1.15 ± 0.94	$6.20^{+6.32}_{-4.42}$	1	1.68	1.58	0.89 ± 0.09	0.60 ± 0.04	-0.17 ± 0.08	0.67 ± 0.04	-0.77 ± 0.09	8.66 ± 0.04	H
19	2.33 ± 0.78	$60.94^{+51.25}_{-56.06}$	3	2.58	2.02	0.41 ± 0.38	0.20 ± 0.06	-0.08 ± 0.37	0.38 ± 0.13	-0.28 ± 0.38	8.92 ± 0.08	H
21	$0.98^{+1.49}_{-0.98}$	$14.40^{+23.22}_{-9.41}$	0	1.09	1.12	0.43 ± 0.09	0.45 ± 0.06	0.14 ± 0.06	0.62 ± 0.04	-0.31 ± 0.09	8.74 ± 0.04	H
26a	$0.64^{+1.97}_{-0.64}$	$10.45^{+22.28}_{-5.24}$	0	1.10	1.92	-0.62 ± 0.05	0.25 ± 0.04	0.99 ± 0.01	1.06 ± 0.01	0.74 ± 0.05	8.36 ± 0.02	H
26b	0.77 ± 0.50	$27.11^{+14.77}_{-15.29}$	3	0.41	1.10	0.21 ± 0.05	0.50 ± 0.04	0.41 ± 0.01	0.76 ± 0.02	-0.09 ± 0.05	8.62 ± 0.03	H
28	$2.34^{+2.07}_{-2.07}$	$24.60^{+55.28}_{-22.66}$	3	2.85	1.82	-0.04 ± 0.19	0.83 ± 0.17	0.99 ± 0.03	1.22 ± 0.07	0.16 ± 0.19	–	S
29	$2.88^{+2.93}_{-2.88}$	$23.34^{+74.03}_{-22.32}$	3	3.61	2.09	0.91 ± 0.25	0.77 ± 0.18	-0.02 ± 0.15	0.84 ± 0.16	-0.79 ± 0.25	8.43 ± 0.25	H
31	–	–	3	2.36	1.64	0.51 ± 0.29	0.38 ± 0.26	-0.01 ± 0.06	0.53 ± 0.18	-0.39 ± 0.29	8.82 ± 0.15	H
32	–	–	3	3.63	1.84	1.18 ± 0.11	1.01 ± 0.09	-0.04 ± 0.05	1.05 ± 0.09	-1.05 ± 0.11	7.96 ± 0.21	L

Table 7. The extinction A_V from Balmer decrement, *SFR*s, important emission line ratios, oxygen abundance in ISM and continuum colors of the low-z galaxies. "nc" means no extinction correction for the emission line fluxes. The uncertainties of the line ratios and metallicity are from the uncertainties of extinction and emission line flux measurements.

Slit	A_V	SFR $M_\odot\ \mathrm{yr}^{-1}$	$\log(\frac{[\mathrm{S\,II}]}{\mathrm{H}\alpha})$	$\log(\frac{[\mathrm{N\,II}]}{\mathrm{H}\alpha})$	$\log(\frac{[\mathrm{O\,III}]}{\mathrm{H}\beta})$	$\log R_3$	$12+\log(\frac{\mathrm{O}}{\mathrm{H}})$	$\frac{C6563}{C4861}$
(1)	(2)	(3)	(4)	(5)	(6)	(7)	(8)	(9)
CFRS								
03^{nc}	–	–	-0.26 ± 0.20	-0.80 ± 0.12	–	–	–	–
09	1.30 ± 0.38	$0.88^{+0.24}_{-0.53}$	-0.54 ± 0.04	-0.47 ± 0.06	-0.40 ± 0.08	-0.55 ± 0.11	9.14 ± 0.08	0.5546
13	0.14 ± 0.15	$0.39^{+0.04}_{-0.04}$	-0.39 ± 0.09	-0.37 ± 0.05	-0.36 ± 0.04	-0.49 ± 0.06	9.10 ± 0.04	0.2778
19	1.18 ± 0.52	$0.50^{+0.18}_{-0.28}$	–	-0.40 ± 0.13	0.25 ± 0.06	0.34 ± 0.08	8.53 ± 0.06	0.4482
21	2.45 ± 0.45	$2.18^{+0.70}_{-1.80}$	-0.37 ± 0.10	-0.69 ± 0.15	0.11 ± 0.09	0.15 ± 0.12	8.66 ± 0.08	0.2514
23^{nc}	–	–	-0.37 ± 0.06	0.16 ± 0.01	–	–	–	–
30	0.62 ± 0.19	$1.69^{+0.23}_{-0.60}$	-0.42 ± 0.10	-0.69 ± 0.05	0.05 ± 0.03	0.06 ± 0.04	8.72 ± 0.03	0.1889
UDSR								
01	0.56 ± 0.17	$0.11^{+0.01}_{-0.04}$	-0.52 ± 0.07	-0.89 ± 0.04	0.44 ± 0.02	0.60 ± 0.03	8.35 ± 0.02	0.3810
06	1.02 ± 0.38	$0.45^{+0.12}_{-0.23}$	-0.25 ± 0.18	-0.21 ± 0.04	-0.05 ± 0.07	-0.07 ± 0.09	8.81 ± 0.06	0.3896
11	0.25 ± 0.16	$0.16^{+0.02}_{-0.03}$	-0.02 ± 0.06	-0.23 ± 0.02	-0.14 ± 0.04	-0.19 ± 0.05	8.89 ± 0.04	0.3608
12^{nc}	–	–	-0.20 ± 0.11	-0.26 ± 0.04	–	–	–	–
13^{nc}	–	–	-0.29 ± 0.19	-0.22 ± 0.07	–	–	–	–
16^{nc}	–	–	-0.30 ± 0.05	-0.65 ± 0.04	–	–	–	–
UDSF								
11	$0.01^{+0.09}_{-0.01}$	$0.09^{+0.01}_{-0.00}$	-0.20 ± 0.04	-0.34 ± 0.01	-0.23 ± 0.03	-0.31 ± 0.04	8.98 ± 0.03	0.3308
15	1.06 ± 0.29	$0.51^{+0.10}_{-0.27}$	-0.50 ± 0.19	-1.03 ± 0.14	0.30 ± 0.04	0.41 ± 0.06	8.48 ± 0.04	0.3887
22^{nc}	–	–	-0.35 ± 0.07	-0.49 ± 0.05	–	–	–	–